Title	Pore propagation directions and nanoporous domain shape in n-InP anodized in KOH
Author(s)	Lynch, Robert P.; O'Dwyer, Colm; Quill, Nathan; Nakahara, Shohei; Newcomb, Simon B.; Buckley, D. Noel
Publication date	2013-04
Original citation	Lynch, R. P., O'Dwyer, C., Quill, N., Nakahara, S., Newcomb, S. B. and Noel Buckley, D. (2013) 'Pore Propagation Directions and Nanoporous Domain Shape in n-InP Anodized in KOH', Journal of The Electrochemical Society, 160(6), pp. D260-D270. doi: 10.1149/2.107306jes
Type of publication	Article (peer-reviewed)
Link to publisher's version	http://dx.doi.org/10.1149/2.107306jes Access to the full text of the published version may require a subscription.
Rights	© 2013 The Electrochemical Society
Item downloaded from	http://jes.ecsdl.org/content/160/6/D260.abstract http://hdl.handle.net/10468/6163

University College Cork, Ireland
Coláiste na hOllscoile Corcaigh

Pore Propagation Directions and Nanoporous Domain Shape in n-InP Anodized in KOH

Robert P. Lynch,[a,b] Colm O'Dwyer,[a-d] Nathan Quill,[a,b]

Shohei Nakahara,[a,b] Simon B. Newcomb [a,e] and D. Noel Buckley [a,b,*]

[a] *Materials and Surface Science Institute, University of Limerick, Ireland*

[b] *Department of Physics and Energy, University of Limerick, Ireland*

[c] *Department of Chemistry, University College Cork, Cork, Ireland*

[d] *Micro & Nanoelectronics Centre, Tyndall National Institute, Lee Maltings, Cork, Ireland*

[e] *Glebe Scientific Ltd., Newport, Co. Tipperary, Ireland*

*E-mail: Noel.Buckley@UL.ie, Phone: +353 61 202902, Facsimile: +353 61 202423

Abstract

Pore propagation during the anodization of (100) n-InP electrodes in aqueous KOH was studied in detail by scanning and transmission electron microscopy (SEM and TEM). Pores emanating from surface pits propagate along the <111>A crystallographic directions to form, in the early stages of anodization, porous domains with the shape of a tetrahedron truncated symmetrically through its center by a plane parallel to the surface of the electrode. This was confirmed by comparing the predictions of a detailed model of pore propagation with SEM and TEM observations. The model considered pores originating from a pit at the (100) surface and propagating along <111>A directions at rates equal at any instant in time. It showed in detail how this leads to domains with the shape of a tetrahedron truncated by a (100) plane. Observed cross sections corresponded in detail and with good precision to

1

those predicted by the model. SEM and TEM showed that cross sections were trapezoidal and triangular, respectively, in the two cleavage planes of the wafer, and TEM showed that they were rectangular parallel to the surface plane, as predicted. Aspect ratios and angles calculated from observed cross sections were in good agreement with predicted values. The pore patterns observed were also in good agreement with those predicted and SEM observations of the surface further confirmed details of the model.

Introduction

The anodic etching of many materials leads to the formation of porous structures. In the case of anodization of metals, such as Al,[1,2] Ti,[3,4] Mg [5] and Fe,[6,7] localized etching may be promoted by the formation of semi-conducting, metal-oxide/hydroxide layers which, due to interlayer forces, may be molded into tubular structures. When semiconducting materials are anodized, localized etching can occur leading to selective removal of material such that the remaining material forms a skeletal structure that encompasses a network of pores. In such a manner, Si,[8-13] SiC,[14-16] Ge,[17-20] Ge/Si alloys,[21] and various II-VI[22-24] and III-V[21-29] compounds (including InP[28-40]) can be made porous.

As explained by Zhang[41] the morphologies of these pores vary in orientation, frequency of branching, type of infilling and extent of the porous structure. In general, each of these aspects of pore morphology is dependent on the material,[42] conduction type,[43,44] doping density[45] and orientation[12] of the substrate; the composition[42,46-48] and concentration[31-33] of the electrolyte; the temperature[31,32] and the applied potential.[32,49,50]

For instance, porous layers form in GaP anodized in aqueous H_2SO_4 solution by the growth of almost hemispherical domains of pores into continuous porous layers. [26,51] Such domains form due to the radial propagation of their pores from pits in the electrode surface. However, pore propagation can also occur along crystallographic directions[52] and changing the electrode potential can change the propagation direction of these pores.[53] Modulation of potential results in modulation of the porosity,[54] which in the case of GaP allows the light-scattering properties to be tuned from weak to extremely strong.[52,55]

3

Similar variations in pore morphology are observed in InP and GaAs. In one of the first observations of porous InP formation, pores with triangular cross sections were reported to form along <111> directions when (111)A-oriented n-InP was anodized in the dark in aqueous HCl via an array of periodic holes in a Si mask.[27,56] Similar pores in both GaAs and InP anodized in HCl[35,57-63] have been observed to propagate along the <111>A directions.* At higher potentials, propagation of such pores deviates from the crystallographic directions[32,49,50] towards the direction of the source of current[29,64] and switching of potential allows alternation between these two regimes of "crystallographically-oriented" (CO) and "current-line-oriented" (CLO) pore propagation.[65-68] The composition of the electrolyte also changes the pore propagation behavior [69,70] *e.g.* InP anodized in acidic liquid ammonia (NH_4^+ in NH_3 liquid) displays pores that spread radially out from their origin.

Research on anodization of III-V materials in KOH is sparse in comparison to anodization in acidic solutions. Nevertheless, some of the initial research on the anodization of GaAs was performed in KOH[71] where pores were observed to be along <111> directions. More recently, electrochemical,[72] photo-assisted[73] and photo-sensitized-open-circuit[74] etching of GaN have been performed in KOH.

Our group has reported[30-40] the development of nanoporosity in highly doped (> 10^{18} cm^{-3}) n-InP anodized in > 1.2 mol dm^{-3} KOH and the first observation of the formation of domains of pores[40] beneath a thin layer of dense InP.[34] Interestingly,

---

* We define the directions of propagation as the directions in which the pore tips move. We define the four <111>A directions as pointing along the bonds from an In atom to the next-nearest P atoms and the {111}A planes as the planes normal to these directions and facing in the same respective directions. We similarly define the <111>B directions as pointing along the bonds from a P atom to the next-nearest In atoms. In some literature reports,[57-63] pore propagation in GaAs and InP anodized in acidic electrolytes is described as being along <111>B directions. However, this appears to be merely a difference in definition: by our definition, these pores propagate along <111>A directions.

chemical etching of pore walls is not observed to take place during anodization in high molarity KOH (> 2.5 mol dm^{-3}); all significant etching occurs electrochemically near the pore tips, resulting in pores of uniform diameters of less than 50 nm. This differs from anodization of InP or GaAs in HCl where tapered pores are observed, less than 50 nm in diameter near their tips and greater than 140 nm near the electrode surface;[75] these pores sometimes cross or intersect, presumably due to chemical etching of the pore walls.[76]

This paper presents results of an investigation of the early stages of pore propagation and the resulting domain shape in the InP-KOH system. A model based on pore propagation along the <111>A directions is used to explain the observed structures and domain shapes, and the predictions of the model are compared quantitatively with the experimental observations.

Experimental

Wafers were monocrystalline, sulfur-doped, n-type indium phosphide (n-InP) grown by the liquid-encapsulated Czochralski (LEC) method and supplied by Sumitomo Electric. They were polished on one side and had a surface orientation of (100) and a carrier concentration in the range 3–6 × 10^{18} cm^{-3}. Crystallographic orientation was indicated by primary and secondary flats marking the natural {011} cleavage planes of the wafer according the European/Japanese system.[77] The manufacturer identified these planes from the 'dovetail' and 'V-groove' etch patterns revealed by a standard wet chemical etch. Thus, the primary flat was chosen so that the {111} plane intermediate in direction between it and the (100) surface plane is a {111}A plane , *i.e.* In terminated. For convenience we will call the plane of the primary flat an α plane,

the secondary flat a β plane and the wafer surface a γ plane. The schematic in Fig. 1 summarizes the various planes and directions.

To fabricate working electrodes, wafers were cleaved into coupons (typically ~5 mm square) along the α and β planes noting their orientation. Ohmic contact was made by alloying indium to the back of a coupon; the back and the cleaved edges were then isolated from the electrolyte by means of a suitable varnish. The electrode area was typically 0.2 cm^2. Prior to immersion in the electrolyte, the working electrode was immersed in a piranha etchant (3:1:1 H_2SO_4:H_2O_2:H_2O) for 4 minutes and then rinsed with deionized water.

Anodization was carried out in 5 mol dm^{-3} aqueous KOH at room temperature in the absence of light using a linear potential sweep at 2.5 mV s^{-1}. A conventional three-electrode cell configuration was used, employing a platinum counter electrode and a saturated calomel electrode (SCE) to which all potentials are referenced. A CH Instruments Model 650A Electrochemical Workstation interfaced to a Personal Computer (PC) was employed for cell parameter control and for data acquisition.

Cleaved α and β cross sections of electrodes were examined using a Hitachi S-4800 field-emission scanning electron microscope (FE SEM) operating at 5 kV, unless otherwise stated. Electron-transparent sections for plan-view and cross-sectional transmission electron microscopy (TEM) examination were prepared using standard focused ion beam (FIB) milling procedures[78] in an FEI 200 FIB workstation. The TEM characterization was performed using a JEOL (2000FX and 2011) transmission electron microscope operating at 200 kV.

Results and Discussion

1. Cross-Sectional Electron Microscopy

Figure 2 shows a typical scanning electron microscopy (SEM) image of a cleaved β cross section (*i.e.* parallel to the secondary flat) through an electrode after anodization in KOH. The anodization was terminated in the early stages, before a continuous porous layer had developed. Triangular porous regions are clearly visible. This shows that, as previously reported,[40] individual, isolated porous domains form in the early stages of anodization. We have shown[40] that each such domain is separated from the surface by a thin non-porous layer and is connected to the electrolyte by a pit which penetrates this near-surface layer. Clearly, the β-plane cross sections through these domains are triangular in shape. Most of the pores in Fig. 2 apparently pass through the plane, appearing as hole-like features, but several pores appear to be in the plane.

Figure 3 shows a typical SEM image of a cleaved α cross section through the same electrode as in Fig 2. A quadrilateral porous region with the shape of a truncated isosceles triangle is observed. Two sides of the quadrilateral are parallel to the surface of the wafer, with the shorter side close to the surface (top). We will refer to this shape as an isosceles trapezoid.* Many pores appear along lines in the plane but some pores passing through the plane appear as holes. The center of the trapezoid's short side is connected by a short channel through the near-surface layer to a pit in the surface. From this channel an in-plane pore P_1 extends to the bottom left-hand corner of the trapezoid and another P_2 extends symmetrically to the right.

---

* The term *trapezoid* is defined differently in American and British usages of English. In this paper, we use the American definition of a *trapezoid* as a quadrilateral with two parallel sides of unequal length. This is a *trapezium* in British usage. The trapezoid in this paper is isosceles, *i.e.* the non-parallel sides are of equal length.

Each of these pores makes an angle of ~35° with the surface and so is along a <111> direction.

As indicated in the experimental section, the {111} plane between the primary flat (α cleavage plane) and the surface (γ plane) of the wafer is a {111}A plane. Likewise the {111} plane between the secondary flat (β cleavage plane) and the surface is a {111}B plane. The corresponding directions (i.e. the normal vectors to these planes) are shown schematically in Fig 1. It is clear from Fig. 1 that the <111>A vectors point downwards from the wafer surface in the α planes and upwards towards the wafer surface in the β planes. Thus P_1 and P_2, which originate at the surface and propagate downwards in an α plane, propagate along <111>A directions (as shown in the inset of Fig. 1). Most of the pores in the region below P_1 and P_2 in the image are parallel to P_1 or P_2 while most of the pores above P_1 and P_2 pass through the plane (i.e. appear as holes). Revisiting Fig. 2, the pores in the plane of the image also appear to be along <111> directions. These correspond to holes in Fig. 3. Conversely, in-plane pores in Fig. 3 correspond to holes in Fig. 2.

Figure 4(a) shows a TEM image of a β cross section of an electrode similar to that in Fig. 2. The porous domain has a triangular outline and is clearly separated from the electrode surface by a non-porous near-surface layer at A. Likewise, the TEM image in Fig. 4(b) of an α cross section shows a trapezoidal domain outline. While the shapes in Figs. 4(a) and 4(b) are similar to those in Figs. 2 and 3, respectively, the interiors of the domain images have different appearances. This is because a TEM sample is a slice of material with finite thickness (<100 nm in this case) and so each image is a two-dimensional representation of a three-dimensional object: a projection on a plane. Thus, the actual pore directions cannot be directly

observed; overlapping pores have the appearance of intersecting, and pores passing obliquely through the plane of the image have the appearance of being in the plane.

Figure 5 shows plan-view TEM images of a thin slice (<100 nm thick) through domains where the slice is parallel to, and includes, the surface of the electrode: *i.e.* parallel to the γ plane and orthogonal to both the α and β planes. Clearly, the cross sections of individual domains are approximately rectangular in shape with a mesh-like internal structure. This will be discussed in Sections 3 and 4.

Thus, it is clear from micrographs such as those in Figs. 2–5 that, in the early stages of anodization, porous domains are formed which have, respectively, trapezoidal, triangular and rectangular cross sections in three orthogonal planes: the α, β and γ planes. This strongly suggests that the domain shape is that of a tetrahedron truncated symmetrically through its center by a plane parallel to the surface of the electrode. The presence of porous domains with such a geometrical shape indicates that pores propagate in preferential crystallographic directions. In the next section, we propose a model for such pore propagation and we show that the domain shapes and pore patterns predicated by such a model are consistent with our electron microscopy observations.

2. Model of Pore Propagation and Domain Formation

If pores did not have preferential directions of propagation, they would propagate radially from their point of origin, as in the case of InP etched in acidic liquid ammonia.[70] If this point of origin was just beneath the surface, hemispherical domains would be formed, similar to those seen for GaP etched in H_2SO_4.[85] As already discussed, Figs. 2 and 3 suggest that pores are oriented along <111>

directions. If pores originating at a surface pit propagated along all eight <111>

directions, the domain formed would have the shape of half a cube (see Appendix A).

However, as already noted, Figs. 2–5 show that α and β cross sections are not

rectangular. Furthermore, Fig. 3 shows that primary pores propagate along <111>A

directions. We therefore suggest that all pores propagate only along the four <111>A

directions. These directions are expected since the fastest etching planes in InP are

generally found to be {111}B, *i.e.* the direction of propagation of the etch front is

generally <111>A.[34,79-84] The mechanism of pore propagation along preferential

directions will be discussed in detail elsewhere.[66,77]

The four <111>A directions may be represented by a set of tetrahedrally

symmetrical vectors. To model the domain shape that would result from <111>A

pore propagation, we first consider the hypothetical case of pores originating from a

point in the bulk of the crystal and propagating along four tetrahedrally symmetrical

directions (the vectors *a*, *b*, *c*, and *d*) at rates that are equal at any instant in time.

After time *t*, these four pores will have reached points which form the vertices of a

tetrahedron. Figure 6(a) shows the orientation of such a tetrahedron *T* with respect to

the crystal directions. Branching along the <111>A directions from the primary pores

will lead to secondary pores and additional branching will lead to tertiary and

quaternary pores that fill the volume of the tetrahedron. The process is described in

detail in Appendix B. Thus, such pore propagation along <111>A directions from a

point in the bulk of the crystal would lead to a tetrahedral porous domain *T*.

Of course, pores originate near the surface rather than in the bulk of the crystal

and therefore the porous domain formed will have the shape of a tetrahedron

truncated by a plane parallel to the surface of the crystal at which the pores originate.

Figure 6(a) shows the case of a (100) plane (a γ plane, EE'FF') containing the point of

origin O of the pores and dividing T into two identically shaped parts Q and R (see Fig. 6(b)). If we consider the region below the plane to be the electrode, then R represents the porous domain. This has a square base GG'HH' at the electrode surface and, in addition, two equilateral triangular faces and two isosceles trapezoidal faces. The pores a and b in the plane ABC'D' grow downwards from the γ plane EE'FF'; therefore ABC'D' is an α plane (see Section 1 and Fig. 1). Likewise c and d are in the plane A'CDB' and grow upwards; therefore A'CDB' is a β plane. Thus, the truncated tetrahedral domain arising from <111>A pore propagation from a point at the (100) surface of a crystal will have the shape and orientation illustrated by R in Fig. 6(b).

2.1. Predicted Shapes of Domain Cross Sections

In this section, we discuss the shape of domain cross sections predicted by the above model in the α, β and γ planes and we quantitatively compare the shapes with those observed microscopically. It can be seen from Fig. 6(b) that the β cross section J'LI' through the center of the domain has the shape of an isosceles triangle; this is represented in Fig. 7(a). The height h of this triangle is half that of the cube that encloses T in Fig. 6(a) and the length w of its base is half the length of the diagonal of a face of the cube. Therefore, $w = h\sqrt{2}$; the leg of the triangle is $s = h\sqrt{\dfrac{3}{2}}$ and makes an angle of $\tan^{-1}\left(\sqrt{2}\right) = 54.74°$ with the base. (Interestingly, these are also the ratios that would be observed for the β cross section through the center of a domain of <100> pores.) All β cross sections that intersect the square base of the domain (GG'HH' in Fig. 6) will be triangles with the same dimensions; β cross sections such as S'WS in Fig. 6(b) that do not intersect the base will be smaller, but similar, triangles as illustrated in Fig. 7(b).

It can be seen from Fig. 6(b) that the α cross section IABJ through the center of the domain has an isosceles trapezoidal shape; this is represented in Fig. 7(c). The trapezoid has the same height h as the triangle J'LI' in Fig. 7(a). Its shorter parallel side IJ (base) has the same length w as the base of the triangle since both are equal to the side of the square GG'HH' in Fig. 6. The longer parallel side AB of the trapezoid has a length $2w$ (since it is a diagonal of the bottom face of the cube in Fig. 6). It is easy to show that the other sides (legs) of the trapezoid are equal in length to the legs of the triangle J'LI' in Fig. 7(a).

The α cross sections that do not pass through the center of the domain (such as MSTN in Fig. 6(b)), also have an isosceles trapezoidal shape as shown in Fig. 7(d). The base has the same length (w) as in the base of the trapezoid through the domain center. It is easy to show that the angles $\angle$MST and $\angle$STN are 54.74° as in the trapezoid in Fig. 7(c) and the triangles in Figs. 7(a) and 7(b). However, its height, h', is less than the height (h) of R.

Figure 7(e) shows a schematic γ cross section at the top of the domain near the surface. As indicated, the square corresponds to GG'HH' in Fig. 6 and so its side has the same length (w) as the base J'I' of the triangle in Fig. 7(a) and the base IJ of the trapezoid in Fig. 7(c). The dotted lines are projections of the underlying domain boundary. If the γ cross section was further from the surface, the domain would appear to be rectangular – similar to the dotted line S'STT' in Fig. 7(e) – rather than square. It follows that, when imaging the projection of a thick slice encompassing

12

only part of a domain, *i.e.* from its base (GG'HH') to a thickness less than the height (*h*) of the domain, the outline shown in Fig. 7(e) should be observed.

2.2. Comparison of Predicted Cross Sections with Experiment

The shapes predicted by the model are clearly in good agreement with the SEM and TEM cross-sectional images. The β cross sections in Fig. 2 and Fig. 4(a) show isosceles triangles as predicted in Fig. 7(a) and the α cross sections in Fig. 3 and Fig. 4(b) show isosceles trapezoids as predicted in Fig. 7(c). Lengths and angles were measured for images in Figs. 2–4. Aspect ratios and angles calculated from these measurements are shown in Table 1 for the images of β cross sections in Figs. 2 and 4(a) along with the corresponding values predicted by the model as discussed above. Likewise, aspect ratios and angles for the SEM image of the α cross section in Fig. 3 (through the center of a domain/pit) are shown in Table 2 along with the corresponding predicted values. It can be seen that there is good agreement between the experimental and predicted values in both tables. This indicates good quantitative agreement of actual domain shapes with those predicted by the model.

As discussed above, β cross sections that do not intersect the base of the domain will also have triangular shapes (*e.g.* S'WS in Fig. 7(b)). These triangles will be similar to, but smaller than, triangles formed by cross sections that intersect the base of the domain (Fig. 7(a)) and in addition their distance from the electrode surface will be greater than the distance of the domain's base from the surface. Such a small triangular porous region relatively far from the surface can be observed in the SEM image in Fig. 2 (marked *X*).   From the distance from the surface to the farthest vertex of *X*, the corresponding domain is estimated to have height *h* = 525 nm and base width *w* = 742 nm. From the height (240 nm) of the triangle we estimate that the

center of the domain is 573 nm from the cross section in Fig. 2. A similar small triangular porous region can be observed in the TEM image in Fig. 4(a) (marked *X*). In this case we estimate that the corresponding domain has height h = 423 nm and base width w = 596 nm and that its center is 490 nm from the TEM cross section.

As discussed in Section 1, the γ cross section in Fig. 5, obtained from a <100-nm-thick TEM specimen at the electrode surface, shows rectangular (almost square) domain shapes. This is in agreement with the shape of the top face of the domain predicted by the model (GG'HH' in Fig. 7(e)). When a thicker (100) slice is examined by TEM, it is possible to view the overall outline of a greater part of the domain (GS'SG'HTT'H' in Fig. 7(f)). If the domain sampled is small enough to be included completely within the thickness of the slice, the overall outline of the domain can be observed (GAG'HBH' in Fig. 7(e)). This can be seen in the TEM image in Fig. 8. The slice thickness is >400 nm, which is thicker than some of the smaller domains at this stage of etching. The domains are longer in one direction and along this direction some domains terminate at points, giving a "ship's deck" appearance, while the larger domains have been truncated by the ion-beam milling procedure during preparation and are therefore similar in outline to Fig. 7(f). By examining the truncation of the larger domains it is estimated that the furthest a domain can extend past the square base in the long direction (*i.e.* u = (ST - MN) / 2) is between 250 and 300 nm giving a slice thickness ($h' = u\sqrt{3}$; see Fig. 7(d) and (f)) of between 430 and 520 nm. These observations further support the proposed model.

Thus, the observed cross sections correspond precisely to those of the truncated tetrahedron predicted by the model for pore propagation along the <111>A crystallographic directions from a point close to a (100) surface.

3. Predicted Pore Patterns and Comparison with Experiment

3.1. Predicted Pore Patterns and Comparison with SEM Images

In this section, we discuss the patterns of pores predicted by the model and compare them with those observed microscopically. The schematic in Fig. 9 shows three porous domains R_1, R_2 and R_3 beneath a (100) surface (γ plane). It also shows the pit from which the domain has formed in each case and the cross sections in α and β planes. As discussed above, α pores propagate downwards along two of the four <111>A directions a and b, and β pores branching from these propagate upwards along the other two <111>A directions c and d. This is shown schematically in R_1. The α cross section shown intersects the domain R_2 through its center forming a trapezoidal shape as discussed above. Pores originating at the surface pit are shown as solid lines extending downwards in diverging directions to the vertices of the domain. Secondary pores in the plane branch from these primary pores; all pores in the plane are parallel to either a or b, *i.e.* they are α pores. This is consistent with the SEM image in Fig. 3 where two such primary pores, P_1 and P_2, extend from a surface pit to the lower vertices of the domain and many other pores are observed in the plane branching in directions parallel to P_1 or P_2.

We note that no point in the region between the primary pores (P_1 and P_2) and the surface is accessible by paths involving only α pores because these propagate downwards only. However, β pores can branch from them and propagate upwards towards the surface in the orthogonal (*i.e.* β) planes. Subsequent branching along β directions allows these pores to thread back through the region between the primary pores and the surface.   In fact, this is the only way that pores can reach that region. The β pores crossing the α cross section are shown as small filled circles in Fig. 9.

Such pores can then branch again to give rise to further α and β pores. This explains the observation that pores above P_1 and P_2 in Fig. 3 mainly pass through the plane (β pores) while pores below P_1 and P_2 are mainly in the plane (α pores). Clearly, the detailed features in Fig. 3 resemble those in the schematic α cross section in Fig. 9 and so are consistent with the model.

The α cross section in Fig. 10 shows an early-stage domain A where the surface pit is intersected by the cleavage plane and a domain B where it is not. Comparing these domains, we see that, while A has primary α pores originating at the pit, the α pores in B originate at through-plane β pores as shown schematically for P_3 in Fig 9. As discussed above, such β pores must have propagated upwards from other α pores that connect them to the surface pit. We also note that the cross section of B has a long edge with less than twice the length of its base (w) and a height $h' < w/\sqrt{2}$ as predicted in Fig. 7(d). Furthermore, some features are visible below the domain image at B that are presumably due to features in more central parts of the same domain underlying the plane of the cross section.

The β cross section shown in Fig. 9 intersects the domain R_3 through its center forming a triangular shape as discussed above. Pores in the plane (β pores) are shown as solid lines extending upwards from where the α pores from which they branched cross the plane. Pores propagating upwards in a β plane can branch downwards in several α planes to form in each case a pattern of pores that is generally similar to that in the α cross section shown. These pores appear as holes where they pass through the β cross section and are shown as small filled circles. The detailed features in Fig. 2 resemble the schematic β cross section: pores appear mainly as hole-like images with fewer in-plane pores. The β cross section shown also passes through R_2 but does

16

not intersect its base. As discussed in Section 3, instances of such cross sections relatively far from the surface can be observed (marked *X*) in the SEM image in Fig. 2 and the TEM image in Fig. 4(a). Thus, the detailed features in the SEM β cross sections resemble the schematic and this further supports the model.

3.2. Comparison of Predicted Pore Patterns with TEM Images

As pointed out in Section 1, the features in the TEM image in Fig. 4(a) are projections of pores in the β plane. Most of the observed features can be divided into two types, called *vertical* (*V*) and *skew* (*S*), represented in Fig. 11 by dotted and solid lines, respectively. Since all pores in any particular α plane will be projected as a line in the β plane of the image, we infer that the vertical *V* features correspond to groups of α pores within the TEM specimen slice. The *V* features in Fig. 4(a) typically have widths of ~35 nm and are generally separated by ~35 nm. These distances correspond approximately to the typical pore widths and inter-pore spacings, respectively, observed by SEM: *i.e.*, in the SEM images of β cross sections (Fig. 2) these planes of pores are viewed as columns of ~35-nm-diameter circles separated by ~35 nm. This suggests that the *V* features correspond to sections of planes of α-pore networks, within the TEM slice and orthogonal to the image plane, separated from each other by approximately ~35 nm; their length in the TEM sample is limited by the thickness of the specimen slice (<100 nm).

The *S* features, represented by the solid-line rectangles in Fig. 11, are oriented at angles of 50-60° to the *V* features. As discussed earlier, β pores in the model make angles of ~35° with a line of intersection of a β and a γ plane: this would correspond to an angle of ~55° between the *V* and *S* features. We therefore infer that the *S*

17

features in Fig. 11 correspond to β pores or groups of β pores. The width of the features is generally ~35 nm, in agreement with the observed pore width. However, since the pores are each in a different β plane, the spacing of the S features (*i.e.*, their combined projections on the β plane of the image) is much less regular than the spacing of the V features. This may also explain why the angles of the S features with the V vary somewhat.

The angular relationship of pores can be seen more clearly if a β cross section is oriented in the TEM so that the viewing direction is along the $-\boldsymbol{a}$ vector (<111>B direction). A TEM image obtained in this way is shown in Fig. 12(a): the images of the pores appear to be at angles of 120° to each other and parallel to the projections of the $\boldsymbol{b}$, $\boldsymbol{c}$ and $\boldsymbol{d}$ vectors on the (111) plane normal to the viewing direction.

The features in the TEM image in Fig. 4(b) are projections of α pores. Two prominent features, F_1 and F_2, extend from the surface to the lower vertices of the domain, each making an angle of ~35° to the surface line in the image plane. The region below F_1 and F_2 is populated with features oriented parallel to F_1 and F_2; the general pattern resembles the pattern of pores observed in SEM images of α cross sections (Fig. 3.) From the orientations of the features in Fig. 4(b), we infer that they correspond to α pores in planes parallel to the plane of the image. Features in the region above F_1 and F_2 do not have as clear an orientation. As discussed earlier, this region is not accessible by paths involving only α pores. As before, the geometrical relationship of pores can be seen more clearly if an α cross section is oriented in the TEM so that the viewing direction is along the $-\boldsymbol{c}$ vector (<111>B direction). A TEM image obtained in this way is shown in Fig. 12(b): the images of the pores appear to

be parallel to the projections of the **d, a** and **b** vectors on the (111) plane normal to the viewing direction.

The features in the plan-view TEM images in Figs. 5 and 8 correspond to projections of both α and β pores on the γ plane. These cross sections show a central elongated feature in each of the domains along the [01$\bar{1}$] direction, corresponding to projections of primary pores (such as P_1 and P_2 in Fig. 9). We will call this central feature the primary feature (*PF*): typically it is longer and more obvious in Fig. 8 (thicker TEM slice) than in Fig. 5. Features parallel to the *PF* correspond to α pores propagating away from the electrode surface in the α plane while features perpendicular to the *PF* correspond to β pores propagating towards it in the β plane. As discussed above, the region between primary pores (such as P_1 and P_2 in Fig. 3) and the surface can be reached only by β pores and so β pores predominate near the surface. In the TEM image of a thin slice therefore, the features predominantly are perpendicular to the *PF* and this can be seen in Fig. 5. In the TEM image of a thicker slice (Fig. 8), pores below and above the primary pores form a mesh of projections parallel and perpendicular to the *PF* corresponding, respectively, to the projections of α and β pores. Thus, the features observed in TEM γ cross sections correspond to the predicted projections of <111>A-oriented pores and this lends further support to the model.

Interestingly, <100> pore propagation would lead to square domain cross sections in the (100) plane, and we erroneously suggested a <100> propagation direction in early presentations.[86,87] However, in that case, the pores in the (100) plane would be parallel to the diagonals of the square rather than being parallel to the sides

as in Fig. 5; also, domain cross sections in the α cleavage planes would be similar to the triangular β cross sections.

4. Surface Imaging

4.1. SEM Observations of the Surface

Figure 13(a) shows an SEM image of the surface of an electrode after anodization. High-energy (20 keV) electrons were used in the incident beam, allowing both the surface and near-surface features of the electrode to be examined by collection of secondary and back-scattered electrons. The lines of intersection of α and β planes with the surface (we call these $\alpha_{\parallel}$ and $\beta_{\parallel}$ lines) are respectively parallel and perpendicular to the [01$\bar{1}$] direction shown. There are numerous small pits in the surface, roughly circular with a typical diameter of ~20 nm. Two short dark stripes extend from most of them along the $\alpha_{\parallel}$ directions. Similar but less pronounced stripes extend from these $\alpha_{\parallel}$ stripes along the $\beta_{\parallel}$ directions so that together they form a rectangular mesh along the <011> axes of the image, similar to the mesh-like features observed in TEM plan views (*e.g.* Fig. 5).

The observed features are images of the sub-surface structure, corresponding to projections of <111>A-oriented pores onto the image plane. As discussed above and shown schematically in Fig. 6, the primary pores originating at the pits are α pores.   They are, therefore, generally closest to the surface and so appear as more pronounced features in the SEM image along the $\alpha_{\parallel}$ directions. In contrast, the β pores originate further below the surface and so appear as less pronounced features along the $\beta_{\parallel}$ directions. Hence the image has an asymmetry which reflects the asymmetry in the sub-surface structure.

20

A similar pattern can be seen in the backscattered SEM image in Fig. 13(b) but the sub-surface features are more prominent than in Fig. 13(a). In addition, it can be seen in Fig. 13(b) that, although $\beta_\parallel$-oriented features are clearly visible, they never extend from pits in the surface. This confirms the model of pores initially propagating downwards from the surface in an α plane before branching into pores that propagate back towards the surface in a β plane.

4.2. Asymmetry in the Distribution of Surface Pits

As mentioned above, Fig. 13 shows additional asymmetry in the structure, particularly noticeable in the backscattered electron image in Fig. 13(b), in that the extent of each porous region is greater along $\alpha_\parallel$ than along $\beta_\parallel$. Correspondingly, pits are closer to each other along $\beta_\parallel$ than along $\alpha_\parallel$. In Fig. 14 the separation of pits along the $\alpha_\parallel$ and $\beta_\parallel$ axes in SEM images similar to Fig. 13(a) is plotted against potential.

The separations between pits along $\alpha_\parallel$ and $\beta_\parallel$ (s_v and s_h, respectively in Fig. 14) initially decrease rapidly until they each reach a plateau value near the first peak and trough in current. This reflects the initial rapid increase in the density of pits which is arrested as domains merge into a continuous porous layer.[30-40] The separation of the pits along $\alpha_\parallel$ is slightly larger than along $\beta_\parallel$ at all potentials. Presumably this asymmetry is due to the domain shape and the propagation of the initial primary pores (as shown in Fig. 13(a)) within an α plane. This is consistent with the elongation of domains in the model and the TEM observations of "ship's-deck" shapes in Fig. 8. Therefore, not only does the preferential <111>A pore propagation lead to sub-surface asymmetries but it also leads to a slightly asymmetric distribution of surface pits.

Conclusions

We have carried out a detailed TEM and SEM study of pore propagation during the anodization of (100) n-InP electrodes in aqueous KOH. Pores originate from surface pits and an individual, isolated porous domain is formed beneath each pit in the early stages of anodization. Each such domain is separated from the surface by a thin non-porous layer and is connected to the electrolyte by its pit, which penetrates this layer. We clearly showed that pores emanate from these points, not in a radial fashion to form hemispherical porous domains, but rather along the <111>A crystallographic directions to form domains with the shape of a tetrahedron truncated symmetrically through its center by a plane parallel to the surface of the electrode. We confirmed this by considering a detailed model of pore propagation and comparing its predictions with our SEM and TEM observations. Cross sections of these domains are trapezoidal and triangular, respectively, in the α and β cleavage planes of the wafer, as observed by SEM and TEM, and rectangular in the γ plane, as observed by TEM.

Considering a model of pores hypothetically originating from a point in the bulk of the crystal and propagating along <111> directions at rates that are equal at any instant in time, we conclude that this would lead to cubic porous domains, the tips of the primary pores along the eight <111> directions forming the vertices of the cube. A similar model for pores propagating along the four tetrahedrally symmetrical <111>A directions leads to tetrahedral porous domains, the tips of the primary pores along the four <111>A directions forming the vertices of the tetrahedron. When pores originate at the surface of the crystal, the resulting porous domains are truncated by the surface plane. Thus, <111>A pore propagation from a pore at the (100) surface leads to domains with the shape of a tetrahedron truncated by a (100) plane; its five

22

faces consist of a square (of side w), two isosceles triangles and two isosceles trapezoids.

The predicted cross sections of these truncated tetrahedral domains in the β plane are isosceles triangles with a base-to-height ratio of $\sqrt{2}$. The base of the triangle has length w when the cross section intersects the square face of the domain; otherwise it is shorter and further from the surface. The corresponding cross sections in the α plane are isosceles trapezoids with the same base angles (54.74°) as the triangles. The short-base-to-height ratio of the trapezoid is $\sqrt{2}$ when the cross section is through the domain center; otherwise it is greater. Cross sections in the γ plane are rectangular, with the width-to-length ratio depending on the depth.

The observed SEM and TEM cross sections in the α, β and γ planes correspond in detail and with good precision to those of the truncated tetrahedron predicted by the model. Aspect ratios and angles calculated from observed cross sections for both triangular and trapezoidal cross sections are in good agreement with predicted values.

The pore patterns observed by SEM and TEM are also in good agreement with those predicted. The model predicts pores to propagate downwards in the α plane in two directions, at angles of ~35° to the surface, and upwards in the β plane at the same angles. The patterns observed in SEM and TEM images of both α and β cross sections are in excellent agreement with this prediction. Plan-view TEM images show pore projections in the γ plane forming a rectangular mesh, in excellent agreement with the predicted patterns.

Surface imaging by SEM lends further support to the model. Numerous small pits are observed, and images of the sub-surface structure, corresponding to projections of <111>A-oriented pores onto the image plane, form a rectangular mesh, similar to that observed in TEM plan views. Features parallel to the α plane are more pronounced than features parallel to the β plane, consistent with the model of pores initially propagating downwards from the surface in an α plane before branching and propagating upwards in a β plane. Pits are observed to be closer to each other along the [011] than along the [01$\bar{1}$] directions, consistent with the predicted direction of elongation of domains and propagation of the initial primary pores within an α plane.

Thus, our study conclusively confirms preferential <111>A pore propagation and explains in detail the formation of truncated tetrahedral domains in n-InP electrodes in the early stages of anodization in aqueous 5 mol dm^{-3} KOH electrolyte.

References

1.   J.W. Diggle, T.C. Downie and C.W. Coulding, *Chem. Rev.*, **69**, 365 (1969)

2.   I.M. Tiginyanu, O. Lupan, V.V. Ursaki, L. Chow and M. Enachi, *Comprehensive Semiconductor Science and Technology* **3**, 396 (2011)

3.   J. M. Macak, H. Tsuchiya, A. Ghicov, K. Yasuda, R. Hahn, S. Bauer, and P. Schmuki, *Curr. Opin. Solid State Mater. Sci.*, **11**, 3 (2007).

4.   R.P. Lynch, A. Ghicov and P. Schmuki, *J. Electrochem. Soc*., **157**, G76 (2010)

5.   M.C. Turhan, R.P. Lynch, H. Jha, P. Schmuki and S. Virtanen, *Electrochem. Commun.* **12**, 769 (2010)

6.   S.P. Albu, A. Ghicov and P. Schmuki, *Phys. Stat. Sol. (RRL)*, **3**, 64 (2009)

7.   S. K. Mohapatra, S. E. John, S. Banerjee, M. Misra, *Chem. Mater.*, **21**, 3048 (2009)

8.   R.L. Smith and S.D. Collins, *J. Appl. Phys*., **71**, 8 (1992)

9.   V. Lehmann, *J. Electrochem. Soc.* **146**, 2968 (1999)

10.   J.J. Kelly and H.G.G. Philipsen, *Curr. Opin. Solid-State Mater. Sci.* **9**, 84 (2005)

11.   T. Osaka, K. Ogasawara and S. Nakahara, *J. Electrochem. Soc.,* **144**, 3226 (1997)

12.   S. Rönnebeck, J. Carstensen, S. Ottow and H. Föll, *Electrochem. Solid-State Lett.* **2**, 126 (1999)

13.   M. Christopherson, J. Carstensen, S. Rönnebeck, C. Jäger, W. Jäger, and H. Föll, *J. Electrochem. Soc.,* **148**, E267 (2001)

14.   A.G. Cullis, L.T. Canham and P.D.J. Calcott, *J. Appl. Phys.*, **82**, 909 (1997)

15.   J.S. Shor, I. Grimberg, B.Z. Weiss, A.D. Kurtz, *Appl. Phys. Lett.*, **62**, 2836 (1993)

16.   A.O. Konstantinov, C.I. Harris, E. Janzen, *Appl. Phys. Lett.*, **65**, 2699 (1994)

17.   O. Jessensky, F. Muller, U. Gösele, *Thin Solid Films*, **297**, 224 (1997)

18.   C. Fang, H. Föll, J. Carstensen and S. Langa, *Phys. Stat. Sol. (a)* **204** (5), 1292 (2007)

19.   F. Cheng, J. Carstensen and H. Föll, *Mater. Sci. Semicond. Process.* **9**, 694 (2006)

20.   C. Fang, H. Föll and J. Carstensen, *J. Electroanal. Chem.* **589**, 259 (2006)

21.   M. Schoisswohl, J.L. Cantin, M. Chamarro, H. J. von Bardelben, T. Morganstern, E. Bugiel, W. Kissinger and R.C. Andreu, *Phys. Rev. B*, **52**, 11898 (1995)

22.   T. Unagami, *J. Electrochem. Soc.*, **127**, 428 (1980)

23.   V.P. Parkhutik, L.K. Glinenko, V.A. Labunov, *Surf. Technol.*, **20**, 265 (1983)

24.   Y.E. Makushok, V.P. Parkhutik, J.M. Martinez-Duart, J.M. Albella, *J. Phys. D: Appl. Phys.*, **27**, 661(1994)

25.   D.J. Lockwood, P. Schmuki, H.J. Labbé, J.W. Fraser, *Physics E*, **4**, 102 (1999)

26.   B.H. Erné, D. Vanmaekelbergh, J. J. Kelly, *Adv. Mater.*, **7**, 739 (1995)

27.   T. Takizawa, S. Arai, M. Nakahara, *Jpn. J. Appl. Phys.,* **33**, L643 (1994)

28.   S. Langa, J. Carstensen, I.M. Tiginyanu, M. Christopersen and H. Föll, *Electrochem. Solid-State Lett.* **4,** G50 (2001)

29.   S. Langa, I.M. Tiginyanu, J. Carstensen, M. Christopersen and H. Föll, *Electrochem. Solid-State Lett,* **3**, 514 (2000)

30.   (a) R.P. Lynch, N. Quill, C. O'Dwyer, S. Nakahara and D. N. Buckley, *ECS Trans.* **50**, xxx *submitted* (2012) "Mechanism that Dictates Pore Width and <111>A Pore Propagation in InP" (b) R. P. Lynch, N. Quill, C. O'Dwyer, S. Nakahara and D. N. Buckley, *J. Electrochem. Soc.,* to be submitted (2013)

31. (a) N. Quill, R. P. Lynch, C. O'Dwyer, D. N. Buckley, *J. Electrochem. Soc.,* to be submitted (2013) *"The Effect of Temperature and KOH Concentration on Pore Formation in InP"* (b) N. Quill, R. P. Lynch, C. O'Dwyer, D. N. Buckley, *ECS Trans.* **50**, xxx *submitted* (2012)

32. (a) N. Quill, R. P. Lynch, C. O'Dwyer, D. N. Buckley, *J. Electrochem. Soc.,* to be submitted (2013) *"Current-line Oriented Pore Growth in InP Anodised in KOH"* (b) N. Quill, R. P. Lynch, C. O'Dwyer, D. N. Buckley, *ECS Trans.* **50**, xxx *submitted* (2012)

33. R. Lynch, C. O'Dwyer, D.N. Buckley, D. Sutton and S.B. Newcomb, *ECS Trans* **2**, 131 (2006)

34. R. Lynch, M. Dornhege, P. Sánchez Bodega, H.H. Rotermund and D.N. Buckley, *ECS Trans* **6,** 331 (2007)

35. R. Lynch, C. O'Dwyer, D. Sutton, S. Newcomb, and D.N. Buckley, *ECS Trans* **6,** 355 (2007)

36. R. Lynch, C. O'Dwyer, N. Quill, S. Nakahara, S.B. Newcomb, and D.N. Buckley, *ECS Trans* **16**, 393 (2008)

37. N. Quill, C. O'Dwyer, R. Lynch, C. Heffernan, and D. N. Buckley, *ECS Trans* **19**, 295 (2009)

38. C. O'Dwyer, D.N. Buckley, D. Sutton, and S.B. Newcomb, *J. Electrochem. Soc.,* **153,** G1039 (2006)

39. N. Quill, R.P. Lynch, C. O'Dwyer and D. N. Buckley, *ECS Trans.* **50**, xxx *submitted* (2012) *"Electrochemical Formation of Ordered Pore Arrays in InP in KCl"*

40. C. O'Dwyer, D.N. Buckley, D. Sutton, M. Serantoni, and S.B. Newcomb, *J. Electrochem. Soc.,* **154**, H78 (2007)

41. X.G. Zhang, *J. Electrochem. Soc.* **151**, C69 (2004)

42. J. Carstensen, M. Christopersen and H. Föll, *Mater. Sci. Eng. B* **69-70**, 23 (2000)

43. M. Christopherson, J. Carstensen, A. Feuerhake and H. Föll, *Mater. Sci. Eng. B* **69,** 70, 194 (2000)

44. U. Schlierf, D. J. Lockwood, M. J. Graham, and P. Schmuki, *phys. stat. sol. (a)* **202**, 1446 (2005)

45. P. Schmuki, L.E. Erickson, D.J. Lockwood, J.W. Fraser, G. Champion and H.J. Labbé, *Appl. Phys. Lett.* **72,** 1039 (1998)

46. J. Carstensen, M. Christopersen, G Hasse and H. Föll, *Phys. Stat. Sol. (a)* **182**, 63 (2000)

47. P. Schmuki, J. Fraser, C.M. Vitus, M.J. Graham, H.S. Isaacs, *J. Electrochem. Soc.* **143,** 3316 (1996)

48. P. Schmuki, D.J. Lockwood, J. Fraser, M.J. Graham and H.S. Isaacs, *Mater. Res. Soc. Symp. Proc,* **431,** 439 (1996)

49. A. Hamamatsu, C. Kaneshiro, H. Fujikura and H. Hasegawa, *J. Electroanal. Chem.* **473**, 223 (1999)

50. H. Fujikura, A. Liu, A. Hamamatsu, T. Sato and H. Hasegawa, *Jpn. J. Appl. Phys.* **39**, 4616 (2000)

51. B.H. Erné, D. Vanmaekelbergh and J.J. Kelly, *J. Electrochem. Soc.*, **143**, 305 (1996)

52. M.A. Stevens-Kalceff, I.M. Tiginyanu, S. Langa, H. Föll and H.L. Hartnagel, *J. Appl. Phys.*, **89**, 2560 (2001)

53. R.W. Tjerkstra, J. Gómez Rivas, D. Vanmaekelbergh and J.J. Kelly, *Electrochem. Solid-State Lett.* **5**, G32 (2002)

54.   I.M. Tiginyanu, S. Langa, L. Sirbu, E. Monaico, M.A. Stevens-Kalceff and H. Föll, *Eur. Phys. J. Appl. Phys.* **27**, 81 (2004)

55.   J. Gómez Rivas, A. Lagendijk, R.W. Tjerksta, D. Vanmaekelbergh and J.J. Kelly, *Appl. Phys. Lett.* **80**, 4498 (2002)

56.   T. Takizawa, M. Nakahara, E. Kikuno and S. Arai, *J. Electron. Mat.,* **25**, 657 (1996)

57.   H. Föll, S. Langa, J. Carstensen, M. Christophersen and I.M. Tiginyanu, *Adv. Mater.* **15**, 183 (2003)

58.   E. Spiecker, M. Rudel, W. Jäger, M. Leisner and H. Föll, *Phys. Stat. Sol. (a)* **202,** 2950 (2005)

59.   S. Langa, J. Carstensen, I.M. Tiginyanu, M. Christophersen and H. Föll. *Electrochem. Solid-State Lett.* **5**, C14 (2002)

60.   M. Christophersen, S. Langa, J. Carstensen, I.M. Tiginyanu and H. Föll, *Phys. Stat. Sol. (a)* **197**, 197 (2003)

61.   S. Lölkes, M. Christophersen, S. Langa, J. Carstensen and H. Föll, *Mater. Sci. Eng. B*, **101**, 159 (2003)

62.   S. Langa, J. Carstensen, M. Christophersen, K. Steen, S. Frey, I.M. Tiginyanu and H. Föll, *J. Electrochem. Soc.* **152**, C525 (2005)

63.   H. Föll, J. Carstensen, S. Langa, M. Christophersen and I.M. Tiginyanu, *Phys. Stat. Sol. (a)* **197**, 61 (2003)

64.   F.M. Ross, G. Oskam, P.C. Searson, J.M. Macaulay and J.A. Liddle, *Philos. Mag. A* **75**, 525 (1997)

65.   H. Tsuchiya, M. Hueppe, T. Djenizian and P. Schmuki, *Surf. Sci.* **547,** 268 (2003)

66. H. Tsuchiya, M. Hueppe, T. Djenizian, P. Schmuki and S. Fujimoto, *Sci. Tech. Adv. Mater.* **5**, 119 (2004)

67. S. Langa, I.M. Tiginyanu, J. Carstensen, M. Christophersen and H. Föll, *Appl. Phys. Lett.* **82**, 278 (2003)

68. S. Langa, M. Christophersen, J. Carstensen, I.M. Tiginyanu and H. Föll, *Phys. Stat. Sol. (a)* **197**, 77 (2003)

69. A.-M. Gonçalves, L. Santinacci, A. Eb, C. David, C. Mathieu, M. Herlem and A. Etcheberry, *Phys. Stat. Sol. (a)* **204**, 1286 (2007)

70. A.-M. Gonçalves, L. Santinacci, A. Eb, I. Gerard, C. Mathieu and A. Etcheberry, *Electrochem. Solid-State Lett.* **10**, D35 (2007)

71. M.M. Faktor, D.G. Fiddyment and M.R. Taylor, *J. Electrochem. Soc.,* **122**, 1566 (1975)

72. E. Harvey, C. Heffernan, and D. N. Buckley and C. O'Raifeartaigh, *Appl. Phys Lett.*, **81**, 3191 (2002)

73. L. Macht, J.J. Kelly, J.L. Weyher, A. Grzegorczyk and P.K. Larsen, *J. Crystal Growth* **273**, 347 (2005)

74. J.J. Kelly, L. Macht, D.H. van Dorp, M.R. Kooijman and J.L, Weyher, *in Processes at the Compound-Semiconductor/Solution Interface*, Editors: P.C. Chang, K. Shiojima, R.E. Kopf, X. Chen, D. Noel Buckley, A. Etcheberry, and B. Marsan, State-of-the-Art Program on Compound Semiconductors XLII, **PV 2005-04**, p. 138 (2005)

75. E. Spiecker, M. Rudel, W. Jäger, M. Leisner and H. Föll, *Phys. Stat. Sol. (a)* **202**, 2950 (2005)

76. S. Langa, J. Carstensen, M. Christophersen, H. Föll and I.M. Tiginyanu, *Appl. Phys. Lett.* **78**, 1074 (2001)

77. http://global-sei.com/sc/products_e/inp/flat.html, last accessed January 17, 2013

78. L. A. Giannuzzi and F. A. Stevie, *Micron.*, **30**, 197 (1999)

79. M. Kappelt and D. Bimberg, *J. Electrochem. Soc.*, **143**, 3271 (1996)

80. P. H. L. Notten, *J. Electrochem. Soc.,* **138**, 243 (1991)

81. I. E. Vermeir, W. P. Fomes, and P. van Daele, *J. Electrochem. Soc.,* **142**, 3226 (1995)

82. D. Soltz and L. Cescato, *J. Electrochem. Soc.,* **143**, 2815 (1996)

83. M. M. Carrabba, N. M. Nguyen, and R. D. Rauh, *J. Electrochem. Soc.,* **134**, 1855 (1987)

84. S. N. G. Chu, C. M. Jodlauk, and W. D. Johnston, Jr., *J. Electrochem. Soc.,* **130**, 2399 (1983)

85. R.W. Tjerkstra, J. Gómez Rivas, D. Vanmaekelbergh and J.J. Kelly, *Electrochem. Solid-State Lett.* **5**, G32 (2002)

86. C. O'Dwyer, D.N. Buckley, V.J. Cunnane, D. Sutton, M. Serantoni and S.B. Newcomb, *Proceedings of State-of-the-Art Program on Compound Semiconductors XXXVII,* 202nd Meeting of The Electrochemical Society, Salt Lake City, Utah, **PV 2002-14**, pp. 259 (ECS, Pennington, NJ, 2004)

87. D.N. Buckley, C. O'Dwyer , R. Lynch, D. Sutton and S.B. Newcomb, *Proceedings of State-of-the-Art Program on Compound Semiconductors XLI*, **PV 2004-06** , pp. 103 (ECS, Pennington, NJ, 2004)

Appendix A: Domain Shape due to <111> Pore Propagation

It is useful to model the domain shape that would result from pores hypothetically originating from a point in the bulk of the crystal and propagating along the <111> directions at rates that are equal at any instant in time. Figure A.1(a) shows an isometric view of the eight <111> directions. After time t, the eight pores will have reached points which form the vertices of a cube as shown in Fig. A.1(a). If a pore branches, the branching point can be treated as the origin of a secondary set of pores and these pores can then branch further. It is found that such branching enables the entire volume of the cube to be accessed by pores and thus allows the domain to be porous throughout. This process is considered in more detail in Appendix B for <111>A pore propagation.

Of course, pores originate near the surface rather than in the bulk of the crystal and therefore the porous domain formed would have the shape of a cube truncated by a plane parallel to the surface of the crystal at which the pores originate. Figure A.1(a) shows the case of a (100) plane containing the point of origin of the pores and dividing the cube into two square prisms. If we consider the region below the plane to be the electrode, then the lower half of the cube represents the porous domain. Thus, pore propagation symmetrically along the eight <111> directions from a pit in the surface should form a porous domain with the shape of a square prism. Its cross-sections in the α and β cleavage planes should both have the shape of a rectangle with width twice its height; such a cross section is shown in Fig. A.1(b) for an α cleavage plane. Note that, as shown, pore propagation in all four in-plane <111> directions would be observed

Appendix B: Domain Shape due to <111>A Pore Propagation

The four <111>A directions may be represented by a set of tetrahedrally symmetrical vectors: a, b, c, and d. As previously shown in Appendix A, it is useful to model the domain shape that would result from pores originating from a point O_1 in the bulk of the crystal and propagating along the directions a, b, c, and d at rates that are equal at any instant in time. After time t, pores a_1, b_1, c_1, and d_1 will have reached points $A_1(t)$, $B_1(t)$, $C_1(t)$, and $D_1(t)$ which form the vertices of a tetrahedron $T_1(t)$ as shown in Fig. A.2(a). If a pore branches, say at $A_1(t_1)$, then this position can be treated as the origin O_2 of a secondary set of pores a_2, b_2, c_2, and d_2 the tips of which form a tetrahedron T_2 with vertices A_2, B_2, C_2 and D_2 as shown in Fig 6(b). We note that $A_2 \equiv A_1$ – since a_2 is simply an extension of a_1 – and B_2, C_2 and D_2 are points on the edges of tetrahedron T_1. Thus whenever pore a_1 branches, a secondary pore propagates so that its tip is always at one of the three edges that intersect at A_1 (*i.e.* A_1B_1, A_1C_1 or A_1D_1) of the growing tetrahedron T_1, as shown in Fig. A.2(c). If a_1 branches multiple times, a set of secondary pores is formed the tips of which are arrayed along A_1B_1, A_1C_1 and A_1D_1. Similarly, branching of b_1, c_1, and d_1 leads to arrays of secondary pore tips along other edges of T_1 (*i.e.* along the set of edges that intersect at the respective primary pore tip). Thus the advancing tips of secondary pores are arrayed along the edges of the expanding tetrahedron T_1.

Similarly, branching from a secondary pore O_2B_2 leads to arrays of tertiary pores the tips of which populate the edges B_2A_1, B_2C_2 and B_2D_2 of the secondary tetrahedron T_2 (see Fig. A.2(d)). Since B_2C_2 and B_2D_2 are lines in faces of tetrahedron T_1, it follows that the advancing tips of tertiary pores branching from O_2B_2 are arrayed along faces of the expanding tetrahedron T_1. Therefore, generalizing

the argument to branching from all secondary pores, the advancing tips of tertiary pores can reach, but do not extend beyond, the faces of the expanding tetrahedron T_1. Since branching of tertiary pores creates an array of pore tips on the faces, it follows that the entire volume of the tetrahedron is porous. If the argument is extended to quaternary and higher order pores, it is found that some of these pores terminate on the faces of T_1 and some within its interior but none extend beyond its faces. In summary, when pores originating at a point in the bulk of a crystal propagate at equal rates along the four <111>A directions, a tetrahedral porous domain T is formed.

Of course, pores originate just beneath the near-surface layer rather than in the bulk of the crystal, and therefore the part Q of the tetrahedron T above this surface (shown in Fig. 6(b)) obviously is not available. The analysis outlined above is applicable to the remaining part R of the tetrahedron by the following argument. Pores in R can be divided into two types – those that propagate along paths entirely within R and those that propagate along paths that lead through Q also. Paths of the latter type must cross from Q to R at some point P. However, since all four propagation directions exist within Q and R, any path from O to P through Q can be replaced by an alternative path that exists entirely within R (simply by selecting the pore displacement vectors in an order such that propagation always stays within R). Therefore, any pore of the type that crosses from Q to R may be replaced by an alternative path entirely within R that branches at P and so R will have the same shape as if all of T had been available. Thus, pore propagation along the <111>A directions from a point in a plane will give rise to a porous domain R with the shape of a tetrahedron truncated by the same plane.

The above analysis is applicable to pore propagation from a point near a crystal surface of any crystallographic orientation, resulting in the formation of a tetrahedron truncated by the bottom of the near-surface layer in question.

TABLES:

Table 1 Comparison of experimental and theoretical ratios and angles for the dimensions of β (triangular) cross sections of porous domains A (left of Fig. 2), B (right of Fig. 2) and C (Fig. 4).

	Side-to-Base Ratio		Angle	
	Left	Right	Left	Right
Triangle A	0.851	0.849	55.35°	54.28°
Triangle B	0.837	0.881	54.93°	53.13°
Triangle C	0.845	0.862	56.04°	53.46°
Mean	0.844	0.864	55.44°	53.62°
Predicted	(0.866)	(0.866)	(54.74°)	(54.74°)

Table 2 Comparison of experimental and theoretical ratios and angles for the dimensions of the α (trapezoidal) cross section of a porous domain in Fig. 3.

	Side-to-Base Ratio			Angle	
	Left	Right	Bottom	Left	Right
Experimental	0.830	0.844	1.99	52.79°	55.64°
Predicted	(0.866)	(0.866)	(2.00)	(54.74°)	(54.74°)

FIGURES:

Fig. 1:

Fig. 2:

Fig. 3

40

(a)

(b)

Fig. 4

(a)

(b)

Fig. 5

(a)

(b)

Fig. 6
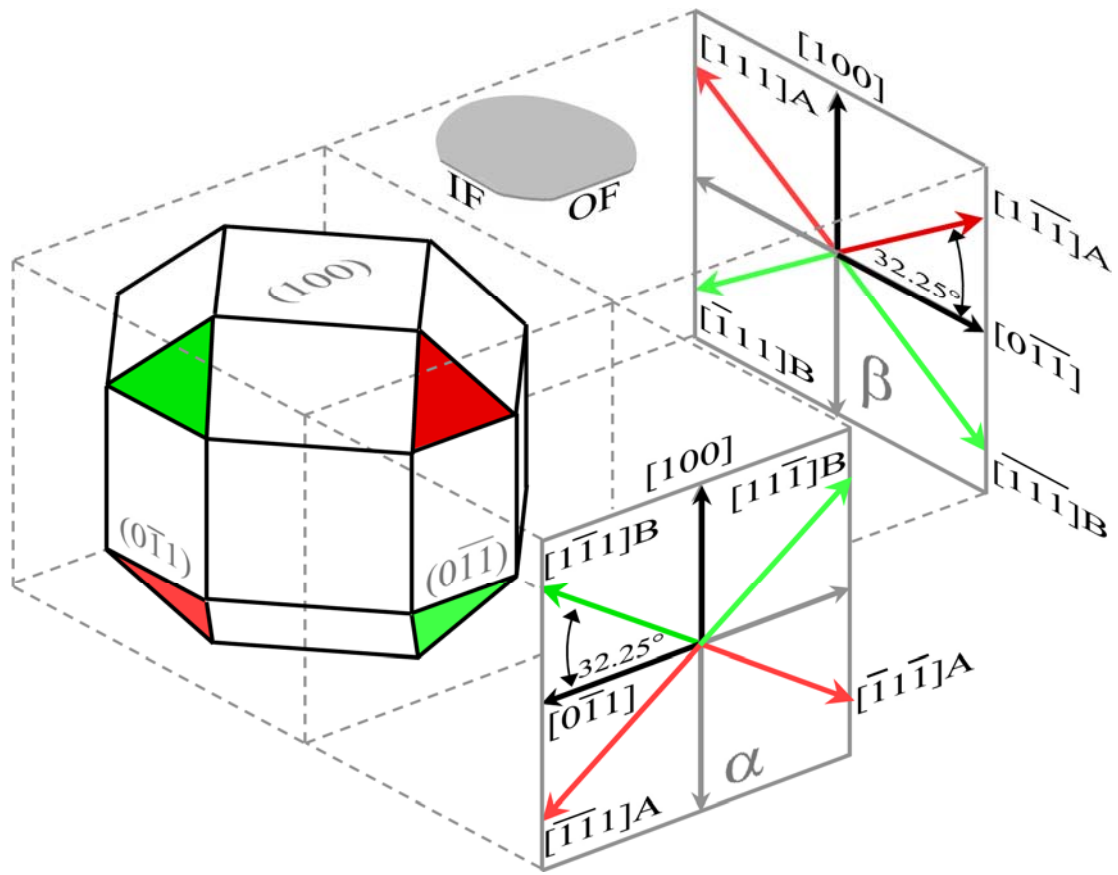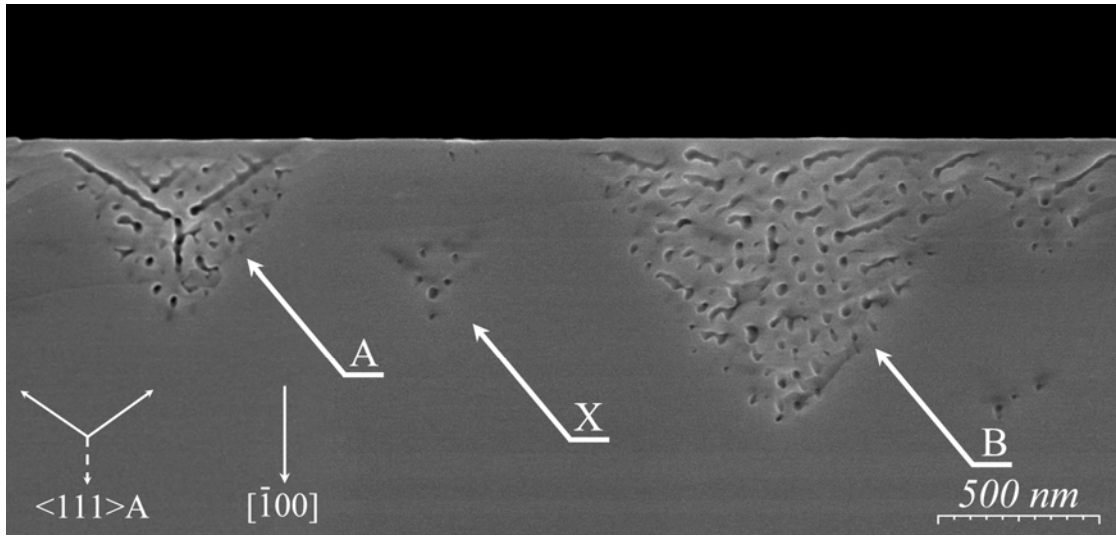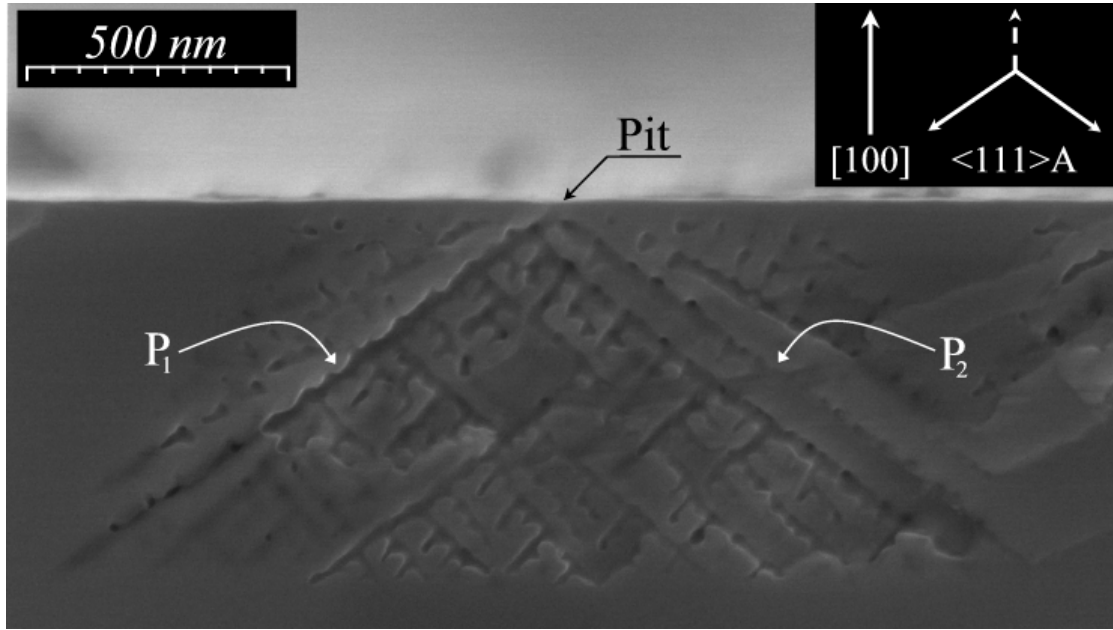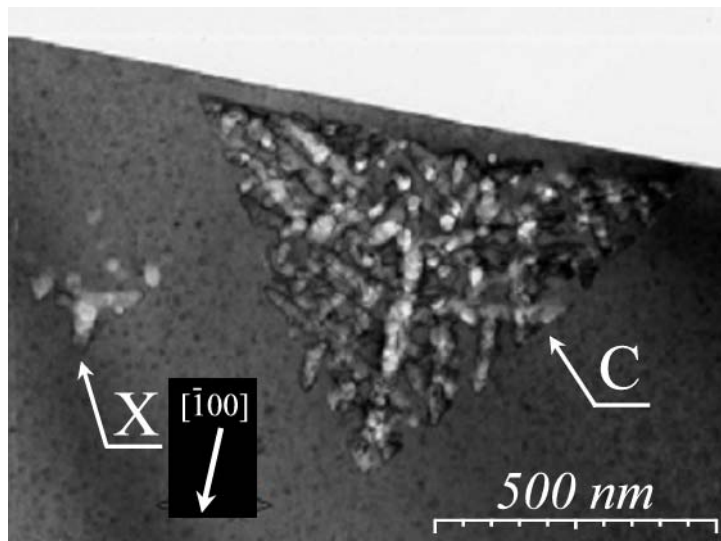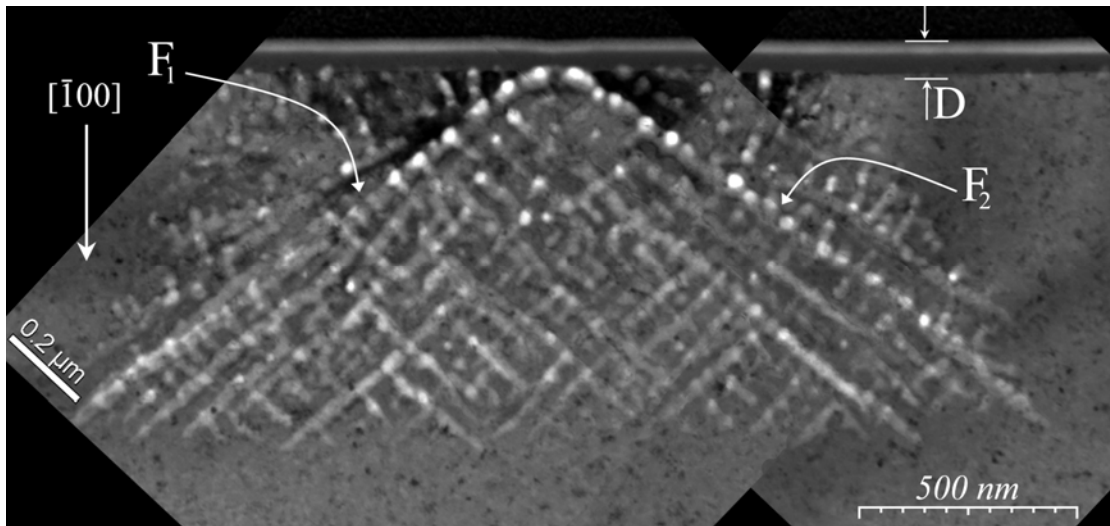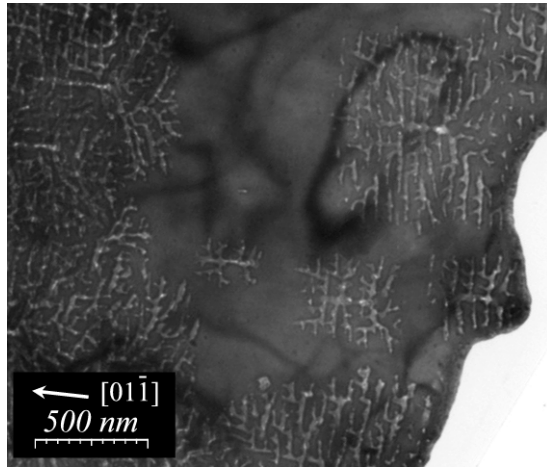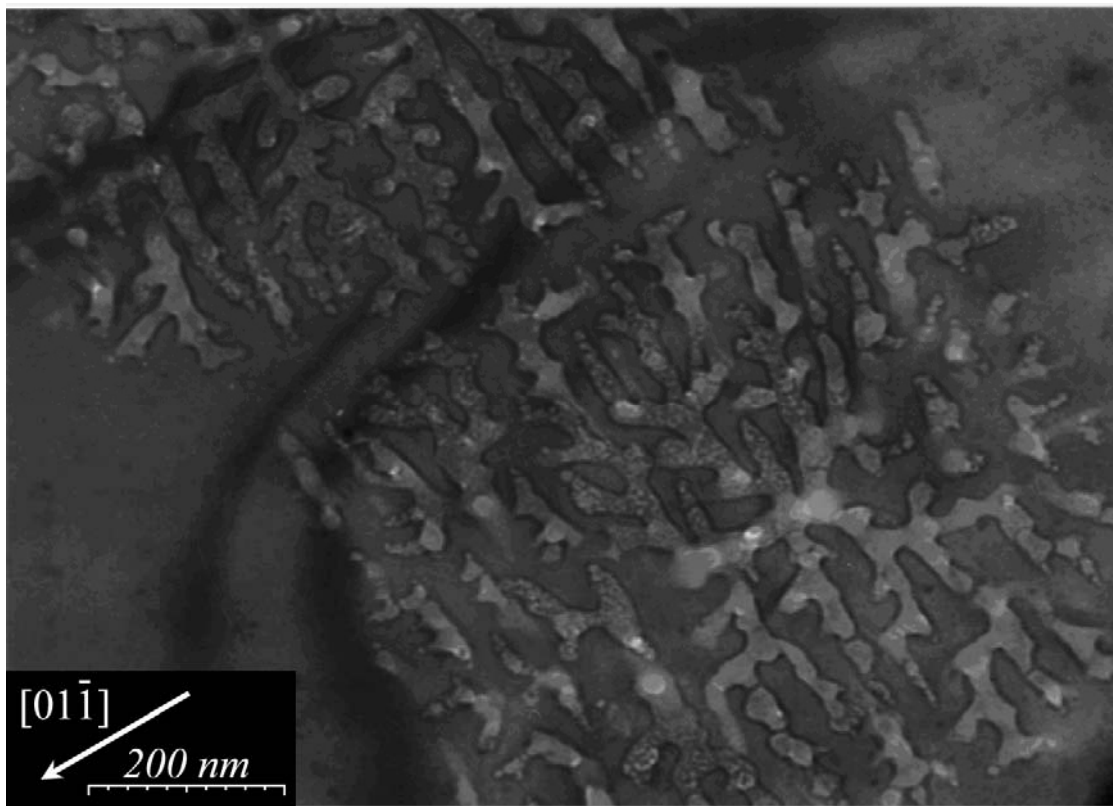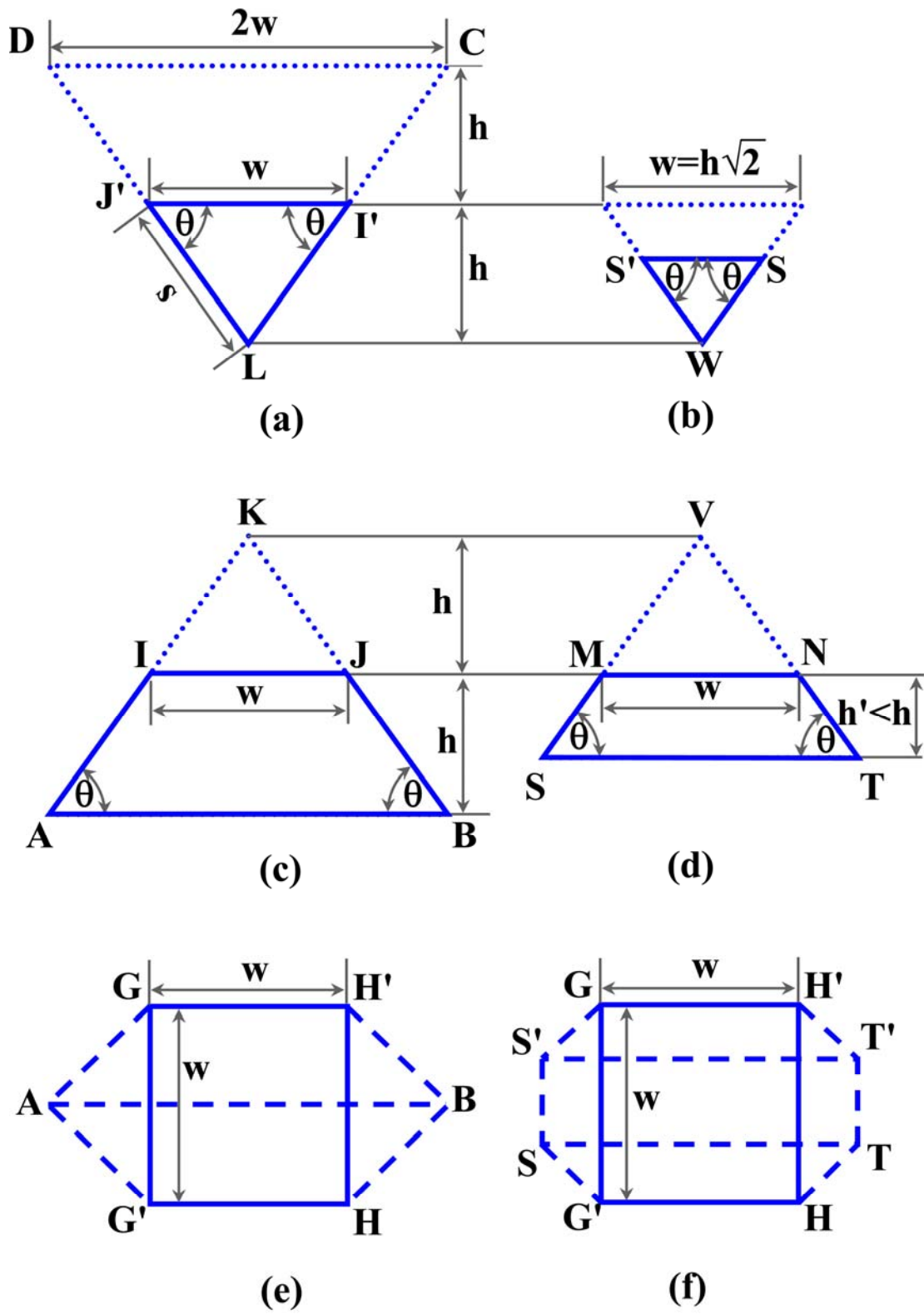
Fig. 7
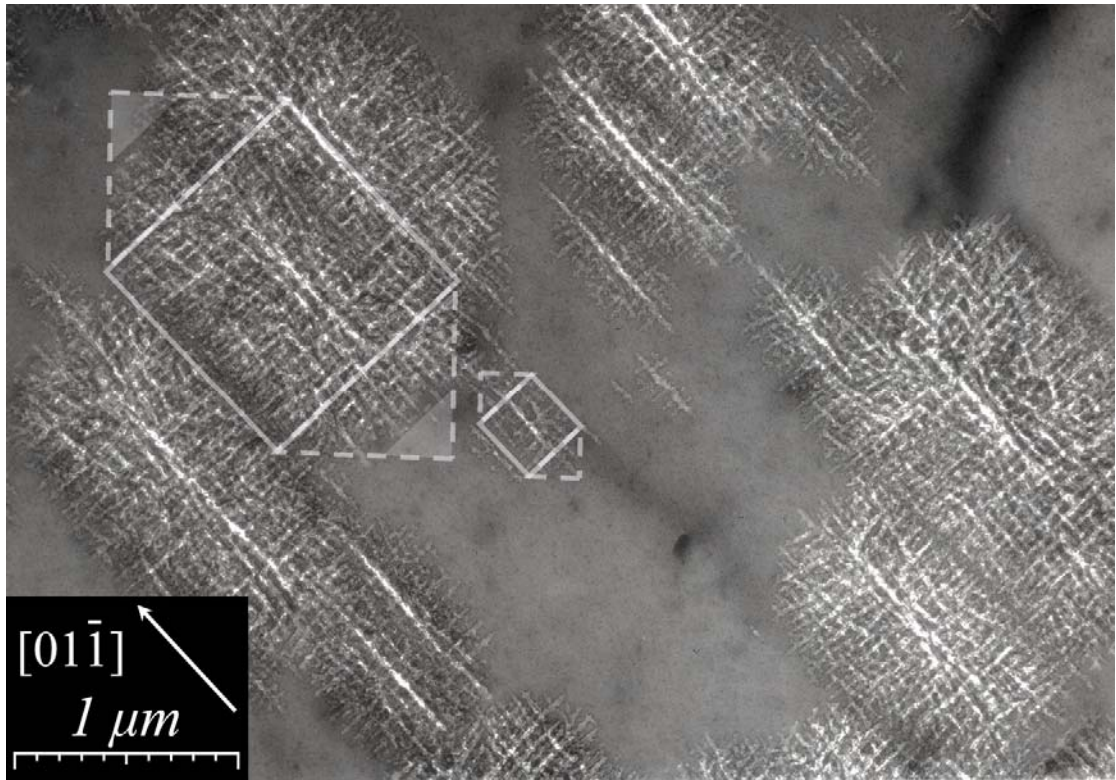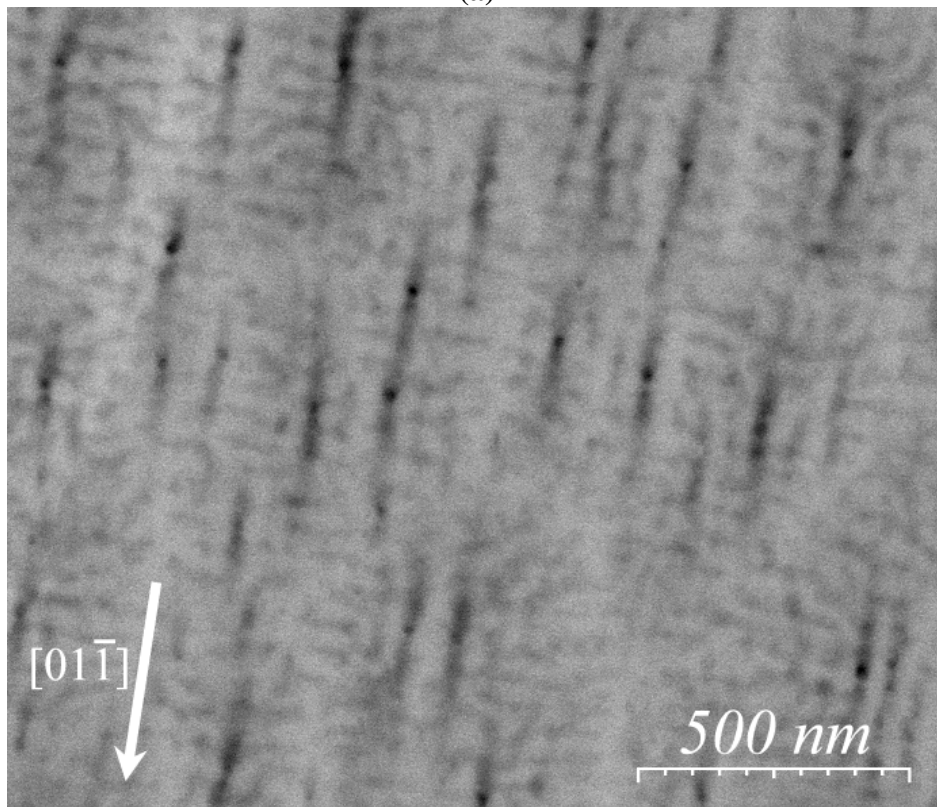
Fig. 8
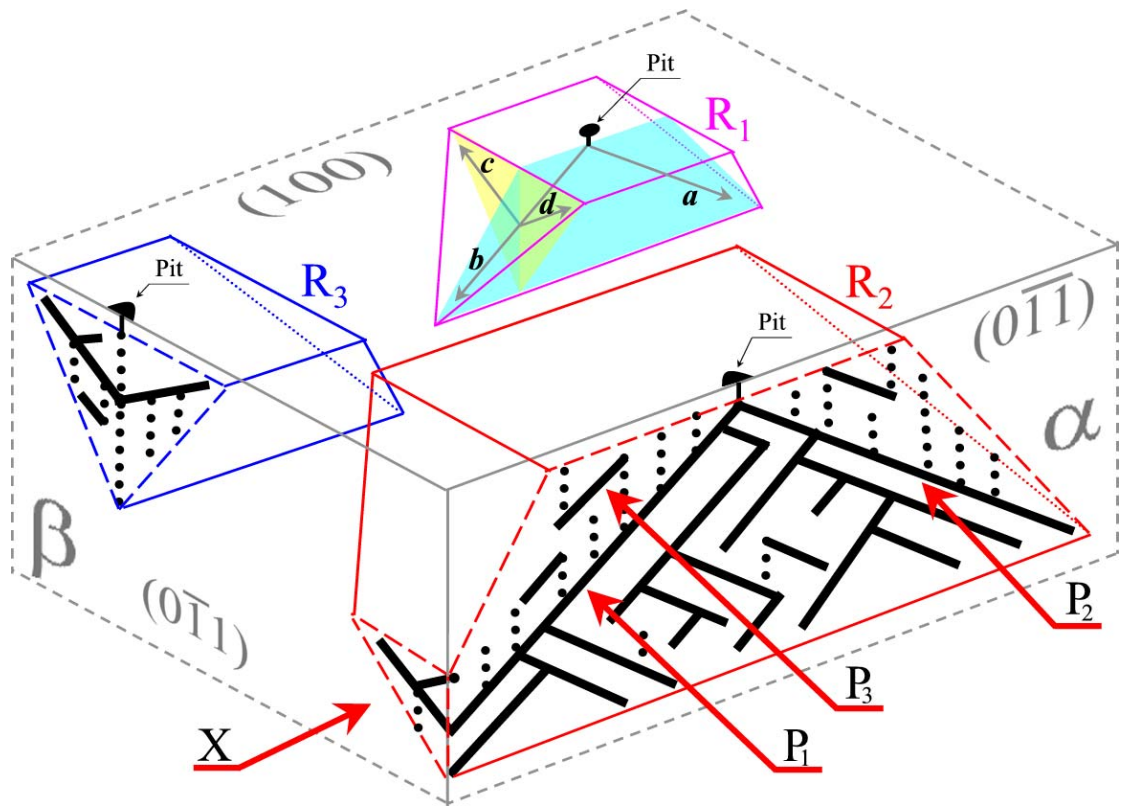
Fig. 9
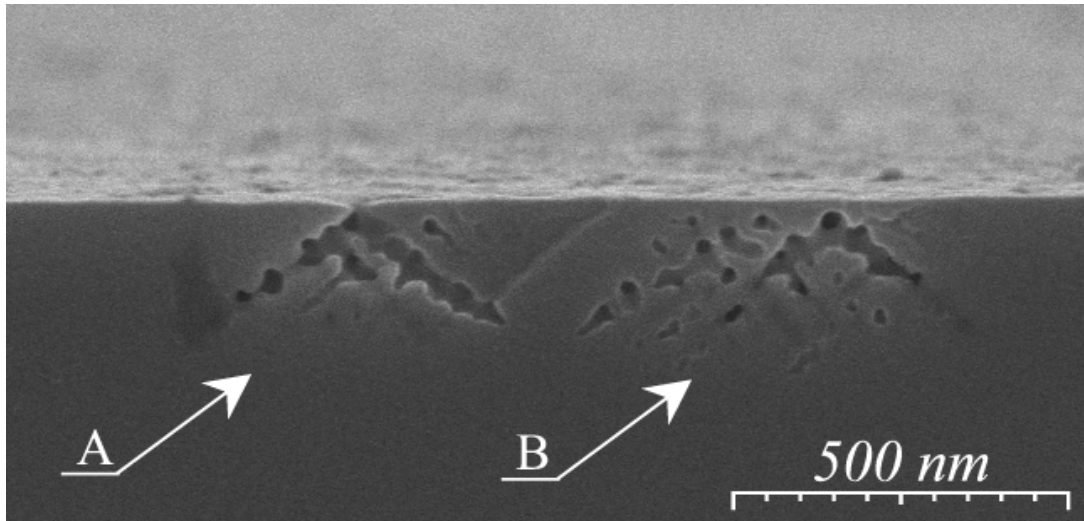
Fig. 10

Fig. 11

(a)

(b)

Fig. 12

(a)

(b)

Fig. 13

50

Fig. 14

(a)

(b)

Fig. A.1

52

<111> A

primary pore

secondary pore

tertiary pore

T₁

D₁

C₁

d₁

c₁

O₁

b₁

B₁

a₁

A₁

(a)

D₂

C₂

d₂

c₂

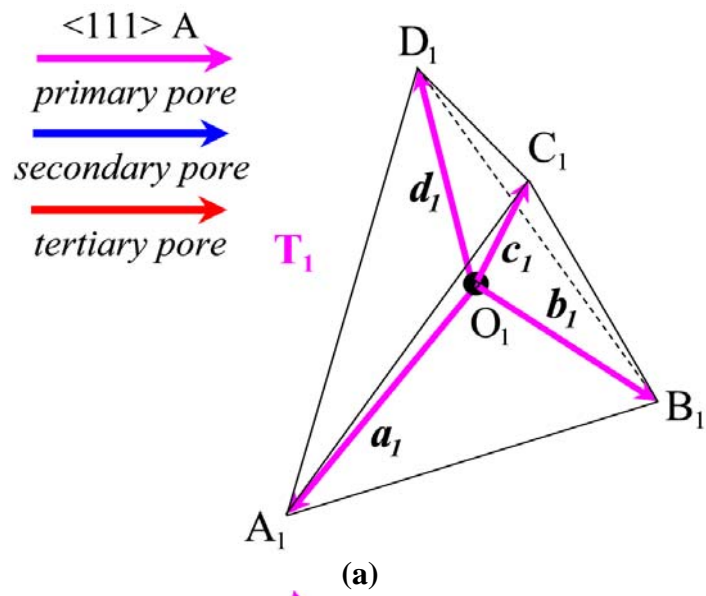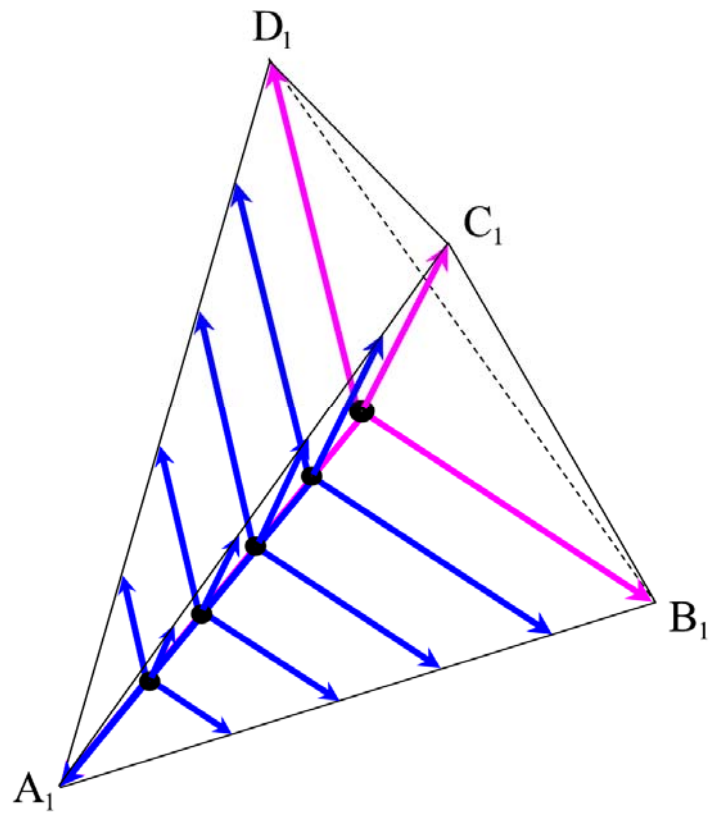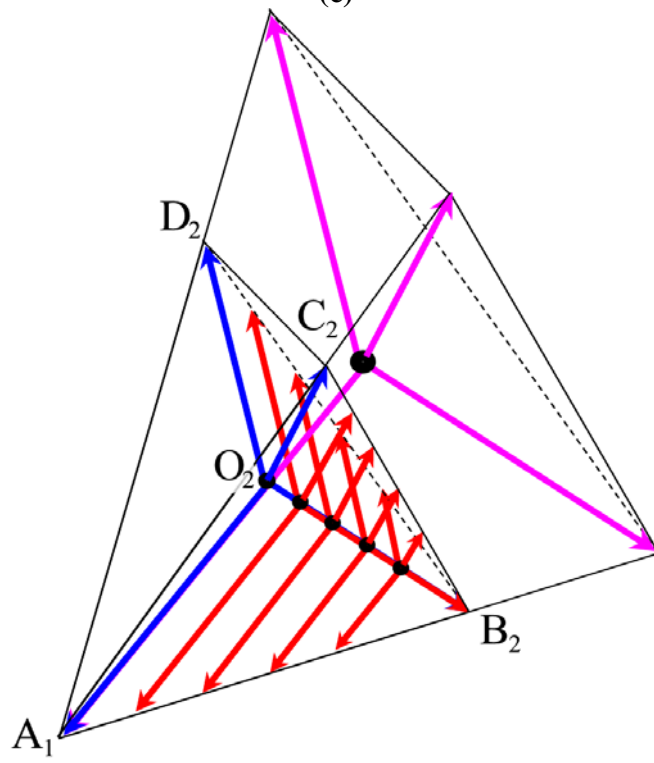T₂

O₂

b₂

B₂

a₂

A₁

(b)

53
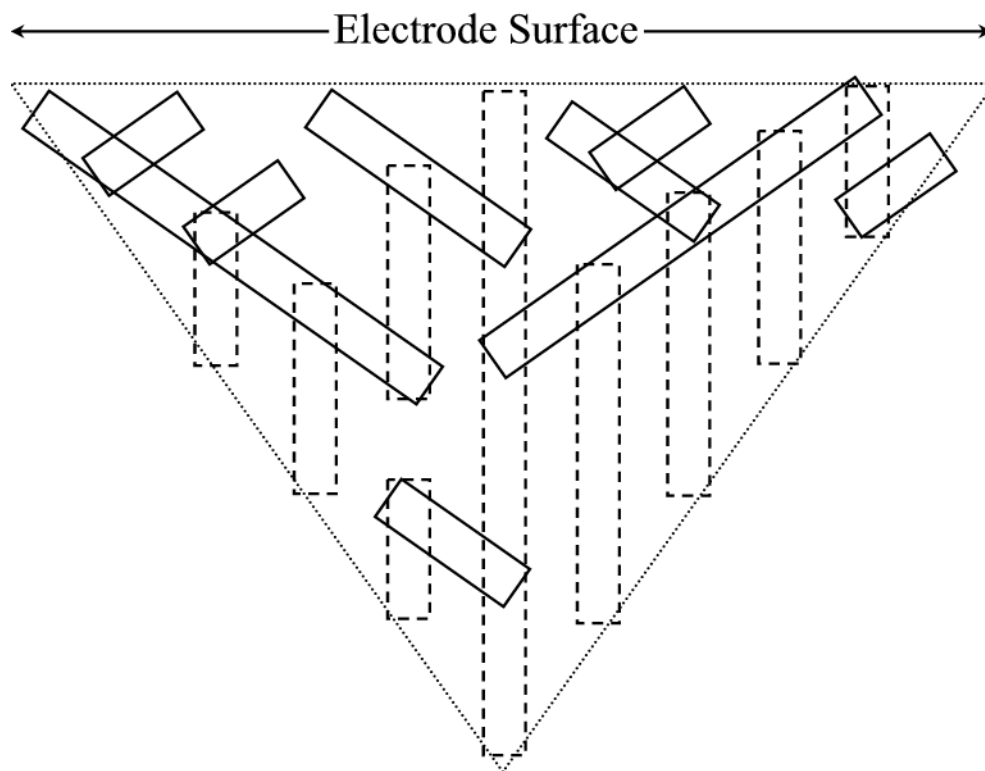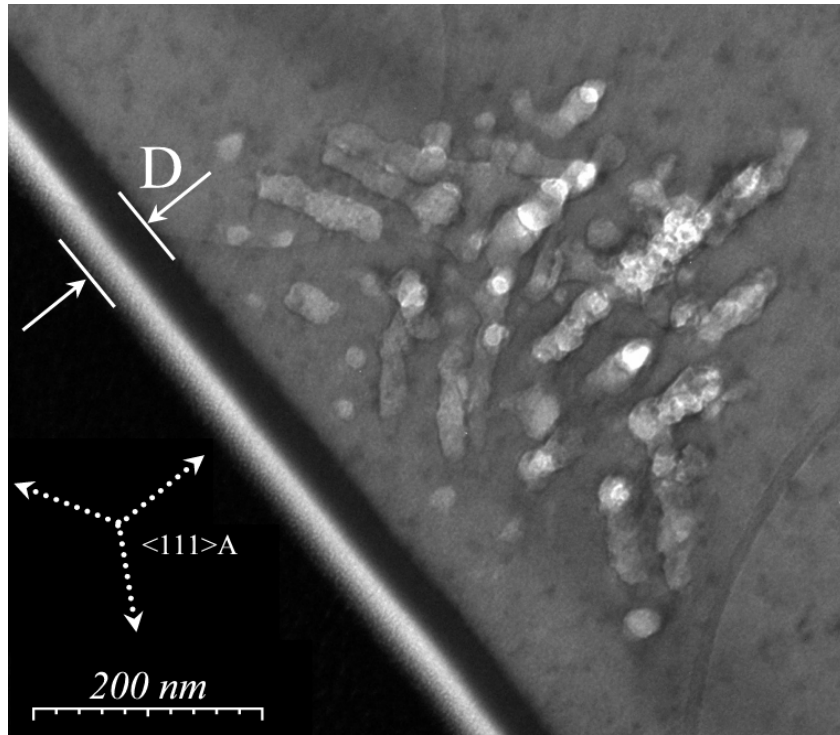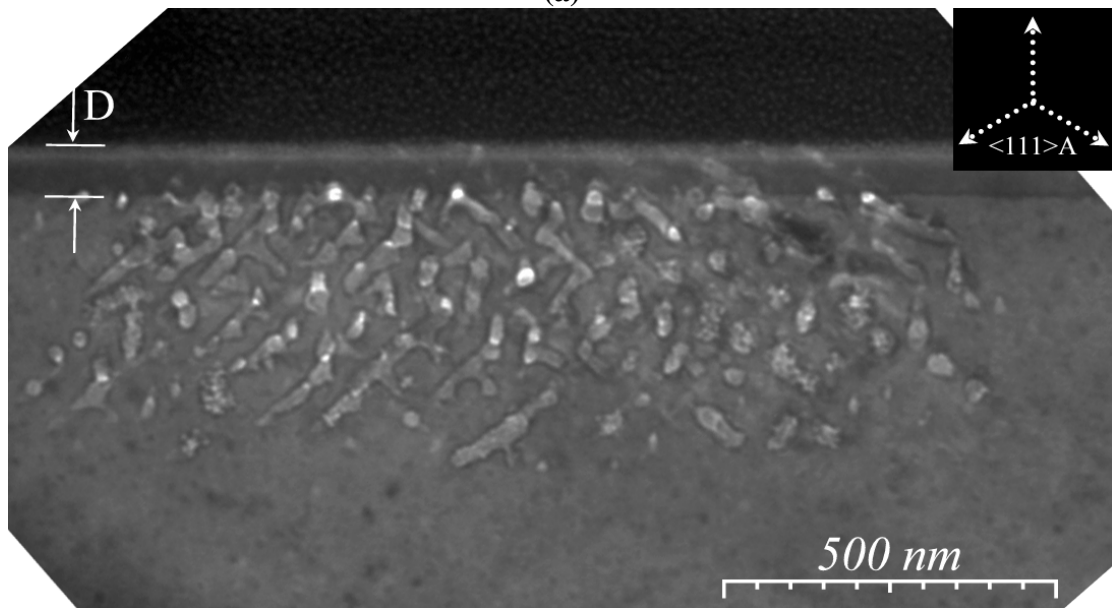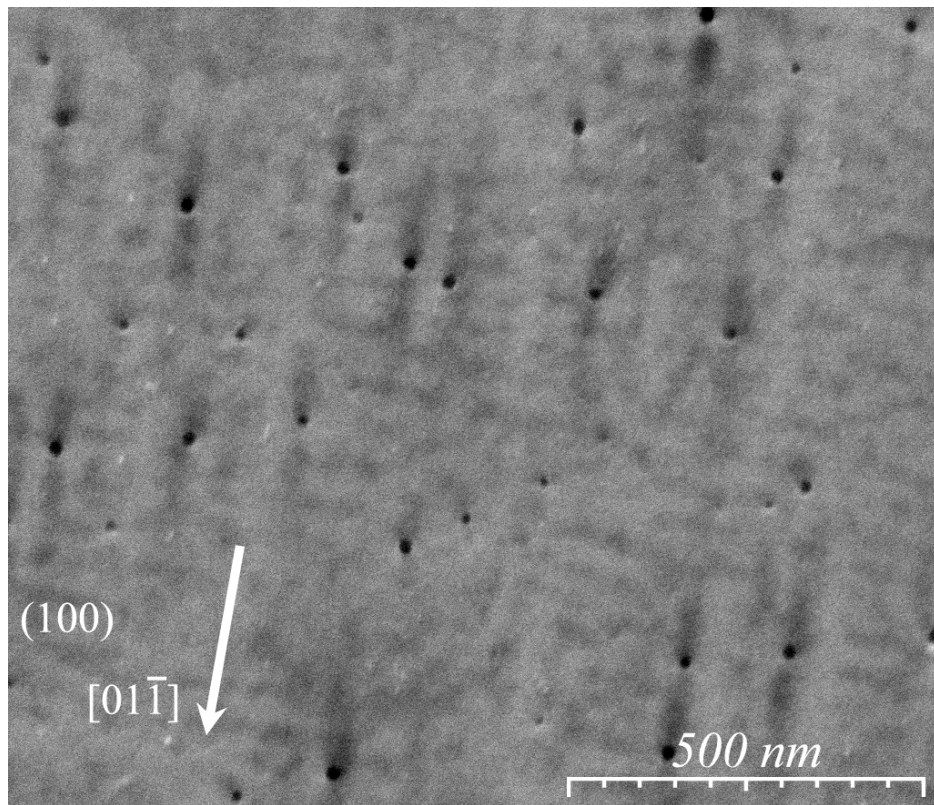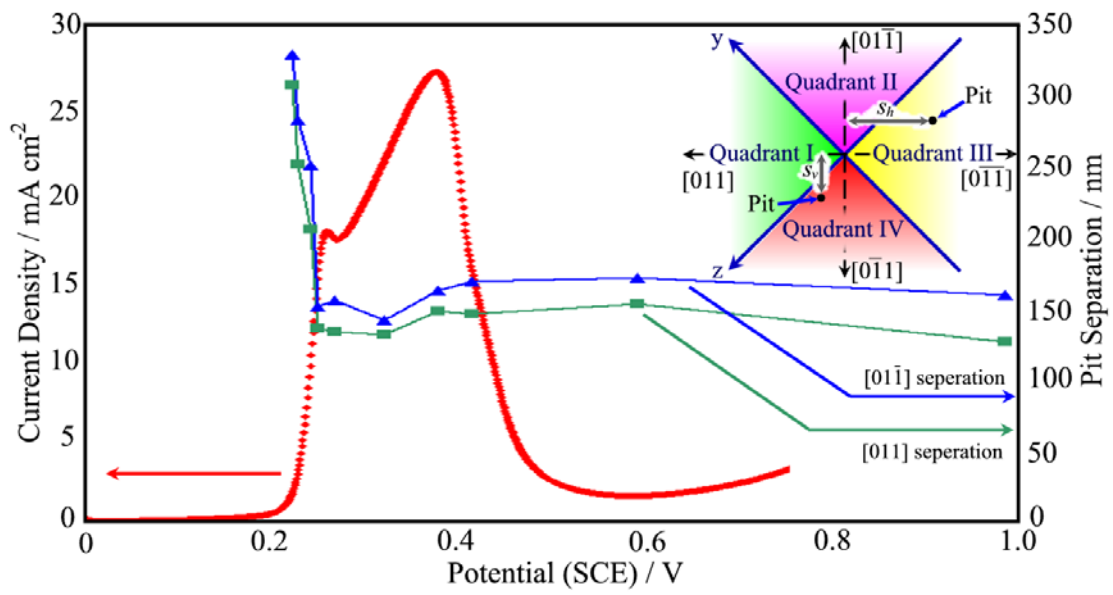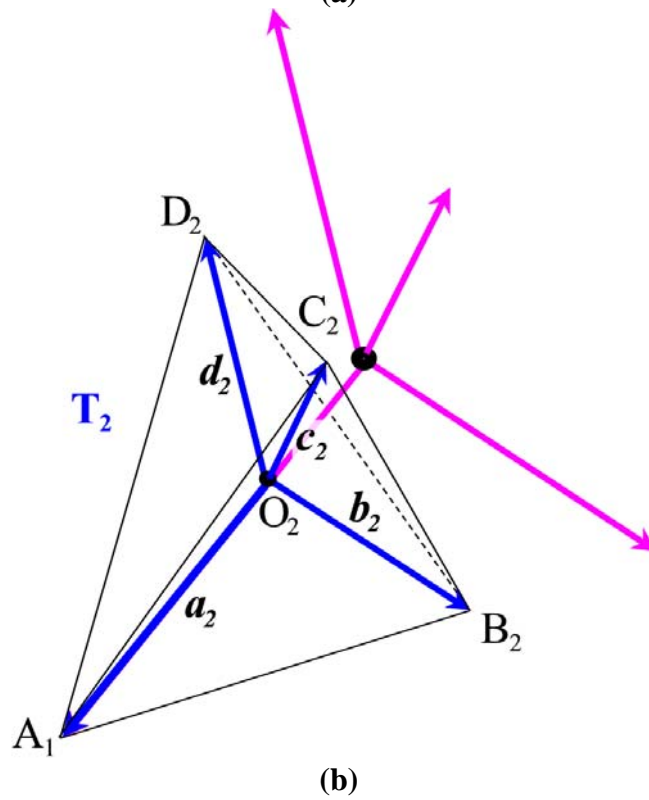
(c)

(d)

Fig. A.2

FIGURE CAPTIONS:

Fig. 1: Isometric drawing showing crystallographic directions and planes relative to the surface and the primary (OF) and secondary (IF) flats of a wafer. We call the primary flat ($0\overline{1}\overline{1}$) an α plane and the secondary flat ($0\overline{1}1$) a β plane. The [$1\overline{1}\overline{1}$]A direction is shown in the β plane and between the [100] and [$0\overline{1}\overline{1}$] directions. This is identified as a [$1\overline{1}\overline{1}$]A direction (*i.e.* In-terminated) from the wafer specification because [100] and [$0\overline{1}\overline{1}$] represent the directions of the surface and primary flats, respectively. Likewise, [$1\overline{1}1$]B is in the α plane and between [100] and [$0\overline{1}1$] as shown.

Fig. 2: SEM image of a cleaved β cross section (*i.e.* parallel to the OF flat) of n-InP after an LPS from 0 V to 0.44 V (SCE) in 5 mol dm^{-3} KOH at 2.5 mV s^{-1}. Triangular domain cross sections can be seen at A and B beneath a thin, non-porous, near-surface layer. Both in-plane pores (line-like features approximately along the <111>A directions shown) and through-plane pores (hole-like features) are evident. The small triangular feature at X corresponds to a domain sectioned far from its center as discussed in the text.

Fig. 3: SEM image of a cleaved α cross section (*i.e.* parallel to the IF flat) of n-InP after anodization under the same conditions as in Fig. 2. A trapezoidal domain cross section can be seen beneath a thin, non-porous, near-surface layer. Both in-plane

pores (line-like features approximately along the <111>A directions shown) and through-plane pores (hole-like features) are evident.

Fig. 4 TEM images of cleaved (a) β and (b) α cross sections of n-InP after anodization under the same conditions as Fig. 2. The TEM slices are <100 nm thick. A triangular domain cross section can be seen in (a) at C beneath a thin, non-porous, near-surface layer. The small triangular feature at X corresponds to a domain sectioned far from its center as discussed in the text. A trapezoidal domain cross section can be seen in (b). The sample in (b) was capped with a carbon deposit (at D) during specimen preparation for TEM. Note also that (b) is a composite of two images of the same domain.

Fig. 5: TEM images of a plan-view (γ) slice of n-InP anodization under the same conditions as in Fig. 2. The TEM slice is <100 nm thick and was obtained by ion-milling upwards towards the surface: its upper face is the electrode surface.

Fig. 6. Schematic representations of the tetrahedron T (corresponding to $A_1B_1C_1D_1$ in Fig. A.2) defined by pore propagation along the tetrahedrally symmetrical vectors $\boldsymbol{a}$, $\boldsymbol{b}$, $\boldsymbol{c}$, and $\boldsymbol{d}$. In (a), the tetrahedron is enclosed by a cube with faces CC′DD′ = (100) = γ plane, AA′CD′ = (010), and A′BC′C = (001). The plane ABC′D′ = (011) contains the downward-pointing $\boldsymbol{a}$ and $\boldsymbol{b}$ and so is an α plane; it intersects T at an isosceles triangle ABK. Likewise the plane DCA′B′ = (0$\bar{1}$1) contains $\boldsymbol{c}$ and $\boldsymbol{d}$ and so is a β plane; it intersects T at an isosceles triangle DCL. The vectors $\boldsymbol{a}$, $\boldsymbol{b}$, $\boldsymbol{c}$, and $\boldsymbol{d}$ correspond to [$\bar{1}$1$\bar{1}$], [$\bar{1}\bar{1}$1], [111] and [1$\bar{1}\bar{1}$] in Fig. 1, respectively. In (b), the γ plane EE′FF′ = (100) is shown intersecting the tetrahedron through its center at the square GG′HH′ to form

two equal, truncated tetrahedrons Q (top) and R (bottom). R corresponds to the porous region as discussed in the text. The α-plane cross section through O intersects R at an isosceles trapezoid ABJI (i.e. truncated triangle ABK) and the β-plane cross section through O intersects R at an isosceles triangle I'J'L (i.e. truncated triangle DCL).

Fig. 7.   Predicted sections through the porous domain R in Fig. 6: (a) an α plane through the center O of the domain; (b) α plane that does not pass through GG'HH' in Fig. 6; (c) β plane through O; (d) β plane that does not pass through O; (e) γ plane projection of a slice of material containing all of R; and (f) γ plane projection of a slice containing the base GG'HH' but of thickness less than the height h. The solid lines represent the domain outlines in cross sections. The broken lines in (e) and (f) represent projections of the underlying domain on the γ plane. The upper-case letters A, B, C etc. indicate the corresponding points in the three-dimensional representation in Fig. 6. Dimensions are shown in terms of the domain height h.

Fig. 8   TEM image of a plan-view (γ) cross section of the n-InP electrode in Fig. 5 for a >400-nm-thick ion-milled slice. The sample was milled towards the electrode surface so that the near-surface layer and bases of the porous domains would not be damaged by the ion beam. Outlines similar to the schematics of Figs. 7(e) and 7(f) are drawn around domains with heights respectively less than and greater than the thickness of the slice.

Fig. 9   Schematic of porous domains R_1, R_2 and R_3 beneath a (100) surface and cross sections in the α and β planes. Domains are separated from the surface by a thin layer

and each domain originates from a pit penetrating this layer. Pores are represented in R_1 propagating along <111>A directions: downwards along $\boldsymbol{a}$ and $\boldsymbol{b}$ in the α plane and upward along $\boldsymbol{c}$ and $\boldsymbol{d}$ in the β plane.   The α cross section intersects R_2 through its center; the β cross section intersects R_3 through its center and R_2 near its vertex (at X). In the cross sections, in-plane pores are shown as solid lines and through-plane pores as small filled circles. P_1, P_2, and P_3 indicate in-plane α pores.

Fig. 10   SEM image of a cleaved α cross section of n-InP after an LPS from 0 V to 0.23 V (SCE) in 5 mol dm^{-3} KOH at 2.5 mV s^{-1}. Trapezoidal domain cross sections can be seen beneath a thin, non-porous, near-surface layer, one (at A) including a pit and the other (at B) without. Both in-plane pores (approximately along the <111>A directions) and through-plane pores are evident.

Fig. 11. Schematic representation of features observed in the TEM image in Fig. 4(a). The broken-line rectangles represent *vertical* (*V*) features (perpendicular to the electrode surface) corresponding to projections of α pores on the plane of the image. The solid-line rectangles represent *skew* (*S*) features, at ~35° to the base of the triangle and ~55° to the vertical, and correspond to projections of β pores. The base of the triangle (top) is parallel to the wafer surface.

Fig. 12.   Cross-sectional TEM images of n-InP slices, <100 nm thick, after anodization under the same conditions as in Fig. 2. The samples were capped with a carbon deposit (at D) during specimen preparation for TEM. In (a) a β-plane TEM slice is tilted so that the viewing axis is along the $\boldsymbol{-a}$ vector: the inset shows projections of the <111>A directions $\boldsymbol{b}$, $\boldsymbol{c}$ and $\boldsymbol{d}$ on the (111) image plane.   In (b) an

α-plane TEM slice is tilted so that the viewing axis is along the **-c** vector: the inset shows projections of the <111>A directions **d**, **a** and **b** on the (111) image plane.

Fig. 13 Plan-view SEM images (taken at an accelerating voltage of 20 kV) of the (100) surface of n-InP after an LPS from 0 V to 0.537 V (SCE) in 5 mol dm^{-3} KOH at 2.5 mV s^{-1}: (a) a secondary-electron image allowing both the surface pits and some sub-surface features to be observed; (b) a backscattered-electron image allowing sub-surface features to be observed to a greater extent.

Fig. 14 Average separation of pits along the $\alpha_\parallel$ and $\beta_\parallel$ axes ([01$\bar{1}$] and [011] directions), in micrographs such as Fig 13, plotted against potential. A linear sweep voltammogram is superimposed for comparison.   Each electrode was anodized by a LPS at 2.5 mV s^{-1} from 0 V (SCE) to the selected potential in 5 mol dm^{-3} KOH. The n-InP had a carrier concentration of 5–5.6 $\times$ 10^{18} cm^{-3}.   As shown in the inset, measurements of pit separation were made by dividing the region of an SEM image around a pit into quadrants along the four <011> directions.   In quadrant III, for example, a pit is shown displaced by s_h along $\beta_\parallel$ from the reference pit; similarly in Quadrant IV a pit is shown displaced by s_v along $\alpha_\parallel$. In each quadrant the pit with the smallest value of displacement (s_h or s_v) was chosen. The values of s_h and s_v were then averaged over all pits.

Fig. A.1 (a) Isometric drawing showing the four <111>A (continuous green arrows) and four <111>B (dashed pink arrows) directions in relation to a (100) electrode surface (a γ plane) and an α cleavage plane (a (011) plane parallel to the primary flat). The cube (dotted line) represents the shape of a domain formed due to pores

originating from a point in the bulk of the crystal and propagating preferentially along all eight <111> directions. (b) Schematic α cross section of a domain due to pores originating from a point at the surface of the crystal and propagating preferentially along all eight <111> directions. The four in-plane <111> directions are shown.

Fig. A.2.   Schematic representation of porous domain formation by propagation of pores from a point in the bulk of a crystal along four <111>A (tetrahedrally symmetrical) directions a, b, c, and d (see Fig. 6). (a) Pores originating from a point O_1 propagate along a_1, b_1, c_1, and d_1 to points A_1, B_1, C_1, and D_1 on the vertices of a tetrahedron T_1; (b) a pore branching at O_2 on a_1 gives rise to a secondary set of pores a_2, b_2, c_2, and d_2 the tips of which form a tetrahedron T_2 with vertices A_2, B_2, C_2 and D_2; (c) Whenever pore O_1A_1 branches, a secondary pore propagates so that its tip is always at one of the edges A_1B_1, A_1C_1 or A_1D_1 of the growing tetrahedron T_1; (d) Branching from a secondary pore O_2B_2 leads to arrays of tertiary pores the tips of which populate the edges B_2A_1, B_2C_2 and B_2D_2 of the secondary tetrahedron T_2.